Photoacoustic Photonic Crystal Fiber Gas Sensor

by

Raymond Chen

S.B. E.E., M.I.T., 2006

Submitted to the Department of Electrical Engineering and Computer Science

in Partial Fulfillment of the Requirements for the Degree of

Master of Engineering in Electrical Engineering and Computer Science

at the Massachusetts Institute of Technology

February, 2007

Author_____   _____
Department of Electrical Engineering and Computer Science
February 2, 2007

Certified by_____   __
Farhad Hakimi
Principal Member of Technical Staff
Charles Stark Draper Laboratory Thesis Supervisor

Certified by_____   _____
Rajeev J. Ram
Engineering

Accepted by_____

Arthur C. Smith
Professor of Electrical Engineering
Chairman, Department Committee on Graduate Theses
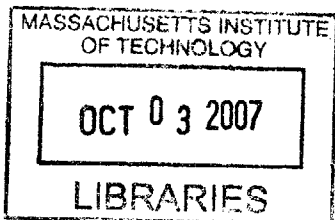
This page intentionally left blank

Photoacoustic Photonic Crystal Fiber Gas Sensor
by
Raymond Chen

Submitted to the
Department of Electrical Engineering and Computer Science

February 2, 2007

In Partial Fulfillment of the Requirements for the Degree of
Master of Engineering in Electrical Engineering and Computer Science

Abstract

Photoacoustic spectroscopy (PAS) is a form of laser spectroscopy that has demonstrated very high sensitivity for gas detection. Typically, PAS involves the absorption of a modulated laser beam by the gas species of interest, and the subsequent generation of acoustic waves at the modulation frequency. The amplitude of the acoustic signal, which can be measured by a microphone, can be amplified by several orders of magnitude with a properly designed gas cell used as an acoustic resonator. In recent times, hollow-core photonic crystal fiber (HC-PCF) has emerged as superior gas cell for standard absorption-based laser spectroscopy due to its small size, compatibility with fiber-based optical components, and easily attainable long light-gas interaction path lengths. However, the possibility of utilizing HC-PCF as a gas cell for PAS has yet to be explored. The size and structure of HC-PCF demands that a new method of PA signal detection must be proposed, because the conventional use of microphones for PAS is not applicable. This thesis describes the development of a proposed novel use of HC-PCF as a PA gas cell from theoretical support to experimental realization. A number of unresolved experimental issues prevented data on the performance of the constructed system from being obtained. These problems are discussed, and recommendations for further study, including several proposed measures to overcome these experimental issues, are made in the conclusion to the thesis.

Technical Supervisor: Farhad Hakimi
Title: Principal Member of Technical Staff, Charles Stark Draper Laboratory

Thesis Advisor: Rajeev J. Ram
Title: Associate Professor of Electrical Engineering, M.I.T.

This page intentionally left blank

Acknowledgements
February 2, 2007

I would like to give thanks to George Schmidt and the Draper Fellow program for the opportunity to work towards the degree of Meng the Master. I would also like to recognize all of the technicians, engineers, and employees at Draper Laboratory who helped me at various stages of the research project. Without their assistance, I would not have made the progress necessary for this thesis, or learned as much from the Meng the Master experience. Special thanks go out to my thesis supervisors Farhad Hakimi and Rajeev Ram for their encouragement and guidance throughout the entire research process. Last, but not least, I would like to thank the men of 5188 for their infinite wealth of entertaining stories. Gentlemen, fight the good fight. I wish you all the best in your future endeavors.

(Author's signature)

5

This page intentionally left blank

Contents

List of Figures

This page intentionally left blank

Chapter 1

Introduction

The research carried out for this thesis was part of an ongoing effort to explore the novel use of hollow-core photonic crystal fiber (HC-PCF) for gas sensing. There exist many applications where it is necessary to know the concentration of a particular gas in a gaseous mixture. Of primary interest are those applications that require the detection of gases whose concentrations are very low i.e. in the ppbv (part-per-billion-by-volume) or sub-ppbv regime. For example, measuring the levels of air pollutants [1], sensing vapors emanating from explosives, drugs, and hazardous chemicals [2, 3], and optimizing the efficiency of industrial processes [4] all need information concerning the trace-level concentration of specific gases that cannot be obtained without gas-sensing techniques of sufficiently high sensitivity. Among the available methods of gas detection, laser-based sensing is especially conducive to high sensitivity [5], as demonstrated by the performance of the various laser spectroscopic techniques that have been developed to date. Furthermore, the fast response times attainable with laser spectroscopy are difficult to match using other methods such as wet chemical analysis, gas chromatography, or mass spectrometry [6]. As a result, novel laser spectroscopic techniques are actively being pursued, particularly as new applications increase the demand for gas-detection sensitivity. The advent of HC-PCF has opened up a wealth of possibilities for laser-based gas sensing that could potentially lead to significantly higher sensitivities.

1.1 Thesis Goals

Although the discovery of the photoacoustic (PA) effect dates back to 1880 by Alexander Graham Bell, photoacoustic spectroscopy (PAS) still remains one of the most sensitive gas-sensing methods in existence today. In PAS, modulated light is absorbed by the gas species of interest and converted to time-varying heat energy. That heat causes the pressure in the gas cell where the gases are held to vary periodically at the modulation frequency i.e. an acoustic signal is produced. Typically, a microphone is then used to detect the acoustic signal. Amplification of the PA signal can be achieved by choosing a modulation frequency that corresponds to an acoustic resonance of the gas cell. This amplification can be as high as several orders of magnitude depending on the nature of the gas cell, and is a major reason why PAS has been able to reach sensitivities in the pptv (part-per-trillion-by-volume) range [7]. In recent years, HC-PCF has been utilized as a gas cell for conventional laser-absorption spectroscopic (LAS) experiments [8]. However, the possibility of its extension to PAS as a novel PA gas cell has yet to be investigated. This idea is not trivial in that the structure and tiny size of HC-PCF precludes the use of microphones as in conventional PAS. The goals of this thesis were to evaluate the theoretical viability of HC-PCF as a PA cell, propose and implement an experimental setup to verify the theory, and obtain preliminary results on its performance i.e. sensitivity, response time, etc.

1.2 Thesis Outline

The main body of this thesis consists of four chapters. Chapter 2 presents information regarding laser-absorption spectroscopy (LAS), wavelength-modulation spectroscopy (WMS), PAS, and HC-PCF. This background chapter serves to elucidate the merits of PAS and HC-PCF. The

theory supporting the idea of using HC-PCF as a gas cell for PAS is discussed in chapter 3. A calculation to estimate the anticipated amplitude of the PA signal is included at the end of the chapter. Chapter 4 details the effort to stabilize the laser wavelength to an atomic absorption line. Both theory and experimental realization are covered. The experimental setup assembled to study the performance of HC-PCF as a PA gas cell is described in chapter 5. Due to unresolved experimental challenges, results were unable to be obtained. These challenges are identified in the last section of the chapter. Finally, recommendations for future work are presented in the conclusion to the thesis.

Chapter 2

Background

The motivation behind the research conducted for this thesis originates from the individual attractiveness of PAS and HC-PCF with respect to laser-based gas sensing. This chapter primarily explains the advantageous features of PAS and HC-PCF for gas detection. There are four sections in the chapter. The first two sections introduce LAS and WMS to establish a basis for comparison with PAS. The third section discusses PAS and its advantages over other absorption-based laser spectroscopic techniques such as LAS and WMS. Finally, the fourth section presents HC-PCF with mention of its application to laser spectroscopy.

2.1 Laser Absorption Spectroscopy (LAS)

Gases absorb light at specific wavelengths. These wavelengths correspond to so-called absorption lines, which collectively form unique absorption spectra that can be used to identify distinct gases. A sample of the near-infrared (NIR) absorption spectrum of methane (CH_4) is shown in Figure 2-1. In many cases, a single prominent absorption line is sufficient to identify a gas species in a gaseous mixture [9]. For example, the absorption line near 1.654 μm in Figure 2-1 could be used to indicate the presence of CH_4. In these circumstances, knowledge of the entire absorption spectrum, or even a large portion of it, is not necessary. This is especially true for situations where there are not gases of similar molecular structure in the gas sample, and the threat of coinciding absorption lines is minimal.
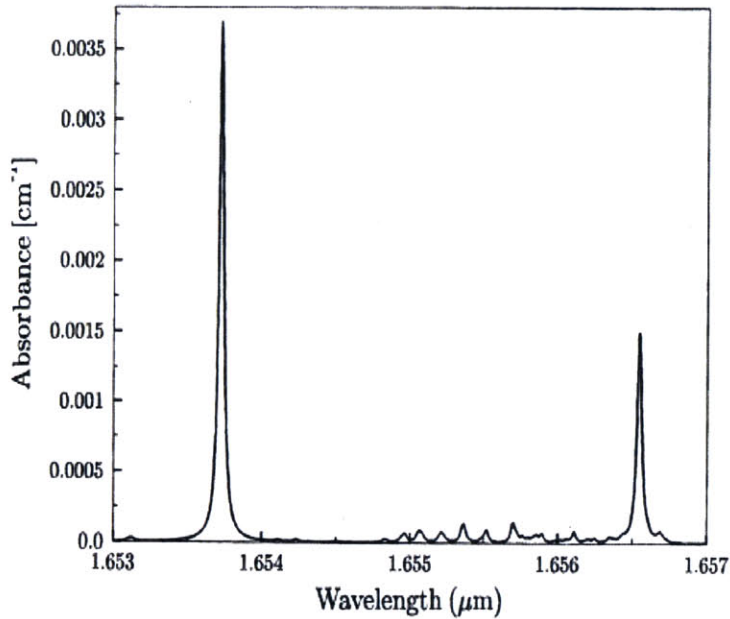
Figure 2-1 Absorption spectrum of CH₄ from 1.653 µm to 1.657 µm [10]

In the absence of coinciding lines, the simplest way to sense a specific gas is to pass light

of a wavelength matching that of a characteristic absorption line through the gas sample

allegedly containing it. If absorption in the form of attenuation is observed in the transmitted

light, then the gas of interest must be present in the gas sample. This detection scheme, referred

to here as LAS, can be implemented with a narrow-linewidth wavelength-tunable laser source,

gas cell, and photodetector [11] as illustrated in Figure 2-2. The laser provides monochromatic

light at an absorption wavelength of the target gas. Any absorption of the light by the gases held

in the gas cell is apparent in the photodetector output as a decrease of signal relative to a

calibrated zero-absorption level.

Figure 2-2 Basic system for LAS

2.1.1 Diode Lasers

Diode lasers are a popular choice as light sources for all types of laser spectroscopy. Fabricated from semiconductor materials, they are low in cost and small in size. In addition, they feature low noise and narrow linewidths [12]. However, the appeal of diode lasers centers on the ease with which they can be wavelength-tuned and modulated at high (GHz) frequencies [13]. Diode lasers are inherently current-driven devices whose output characteristics also depend on the operating temperature. Wavelength tuning can be achieved by adjusting either the injection current or temperature of the laser [12]. Both methods are realizable using commercial equipment; a number of current sources and temperature controllers designed specifically for diode lasers exist. For continuous tuning, distributed-feedback (DFB) or distributed-Bragg-reflector (DBR) diode lasers are optimal. These special diode lasers incorporate optical feedback to prevent mode hopping, the cause of tuning discontinuities and hysteresis in unmodified lasers [12]. On the other hand, wavelength modulation is done solely with the laser current. A modulated component can be superimposed on the bias current by supplying an AC voltage signal to the external modulation input of the diode laser current source, or for high-frequency (> 1 MHz) modulation, a bias-tee network.

Diode lasers can be classified into two main types: gallium-arsenide (GaAs) or indium-phosphite (InP) lasers and lead-salt lasers. GaAs or InP-based diode lasers are operated near room temperature, and have relatively high output powers on the order of milliwatts. Unfortunately, they emit light predominantly in the NIR region of the electromagnetic spectrum ($\approx 0.75\text{-}2.5$ μm) where gases either lack or possess weak absorption lines. In contrast, lead-salt diode lasers emit light in the fingerprint IR region ($\approx 2.5\text{-}25$ μm) where absorption features are up to several orders of magnitude stronger than those in the NIR. However, lead-salt lasers

require cryogenic cooling during operation, and suffer from low output powers on the order of hundreds of microwatts [11]. Due to the advancement of 1.2-2 μm GaAs and InP-based diode lasers brought about by the telecommunications industry, the relative infancy of 3-30 μm lead-salt diode lasers, and the convenience of near-room-temperature operation, absorption-based laser spectroscopic experiments are commonly performed in the NIR despite weak absorption lines [14-18].

2.1.2 Beer-Lambert Law

The Beer-Lambert law, also referred to as the Lambert-Beer law or just simply Beer's law, relates the incident and transmitted light intensities, I_0 and I in Figure 2-2, for conventional LAS. The empirical relationship is given by [19]

$$\frac{I}{I_0} = e^{-\alpha L} \tag{2-1}$$

where α (m^{-1}) is the absorption coefficient or absorbance which represents the rate of absorption through the light-gas interaction path length L (m). The absorption coefficient itself can be expressed as [20]

$$\alpha = \sigma N \tag{2-2}$$

where σ (m^{-2}) is the absorption cross-section of the absorbing gas species and N is its volumetric concentration (m^{-3}). The absorption cross-section is a measure of the absorption of a particular wavelength of light by an individual molecule of the absorbing gas. Since σ strictly depends on the identity of the gas, it can be experimentally determined in advance, and used to calculate the concentration of the gas N following measurements of the light intensities I_0 and I and path length L in a LAS setup.

From (2-1), it is evident that the sensitivity of LAS governed by the Beer-Lambert law is improved by having longer light-gas interaction path lengths. Furthermore, it is apparent that the sensitivity can be enhanced by selecting stronger absorption lines i.e. larger absorption cross-sections for experimentation, although there could be considerably less flexibility in changing σ depending on the wavelength-tuning range of the employed laser source. As the absorbing gas concentration approaches trace levels, the dependencies of the sensitivity on α and L become linear [19]:

$$\frac{I}{I_0} = 1 - \alpha L \tag{2-3}$$

(2-3) can be rewritten in another form which better suits the definition of sensitivity:

$$\frac{\Delta I}{I_0} = \frac{I_0 - I}{I_0} = \alpha L \tag{2-4}$$

2.1.3 Detection Limits of LAS

LAS, as depicted in Figure 2.2, usually fails to meet the sensitivity demands of trace-gas detection. While applications such as monitoring concentrations of atmospheric trace species require sensitivities in the ppb or sub-ppb regimes, LAS systems, outside of a few exceptions, achieve detection sensitivities in the ppm range [20]. The fundamental problem confronting LAS is the accurate measurement of a very small differential signal that is buried under a large background signal. In (2-4), $I \approx I_0$ and $\Delta I = I_0 - I \approx 0$ if the concentration of the absorbing gas is very low. Therefore, it is difficult to sense the change in the transmitted light intensity I resulting from absorption, especially in the presence of fluctuations in the laser output power [19]. In addition, there exist light scattering mechanisms and sources of wavelength-independent

absorption that can complicate the extraction of the gas concentration from the Beer-Lambert law [20].

To improve the sensitivity of LAS, various methods have been employed, mainly seeking to attain long absorption path lengths. This task is challenging because the required interaction path lengths for detection of gases with concentrations in the ppb range or lower are on the order of hundreds of meters [20]. As an alternative, wavelength-modulation spectroscopy (WMS) was developed as a modified LAS technique.

2.2 Wavelength Modulation Spectroscopy (WMS)

The word "line" creates the misconception that absorption lines are infinitesimally narrow in width i.e. purely monochromatic. In reality, some finite linewidth is always apparent [19]. The shape of an absorption feature is determined mainly by the pressure of the gas. Although a detailed discussion on the various line-broadening mechanisms is beyond the scope of this thesis, it is worth noting that absorption line profiles are typically Gaussian in shape at pressures less than 10 Torr, Lorentzian at pressures greater than 100 Torr, and a convolution of both, known as Voigt, at pressures in between 10 and 100 Torr [20].

WMS takes advantage of the absorption lineshape to produce a characteristic detection signal. The experimental setup for WMS is shown in Figure 2-3. In WMS, a modulation signal is superimposed on the laser wavelength. As the operating point wavelength is scanned, a lock-in amplifier demodulates the phase-sensitive amplitude of the photodetector output signal component at the modulation frequency (first harmonic or 1f) or twice the modulation frequency (second harmonic or 2f). In the event that the sweep of the wavelength traverses an absorption line, the corresponding signal measured by the lock-in amplifier will have a distinct shape as a

19

function of wavelength. If the lock-in amplifier is configured for $1f$ detection, then the shape of the signal will resemble the first derivative of the absorption line profile as illustrated in Figure 2-3. Similarly, if the lock-in amplifier is configured for $2f$ detection, then the shape of the measured signal as a function of wavelength resembles that of the second derivative of the absorption lineshape.

WMS improves upon conventional LAS by shifting detection to higher frequencies, thereby reducing the $1/f$ noise of the system [20]. This benefit is more apparent when the lock-in amplifier is used for $2f$ detection as compared to $1f$ detection. In addition, the use of lock-in detection effectively eliminates the large background signal that is particularly troublesome in LAS [20].
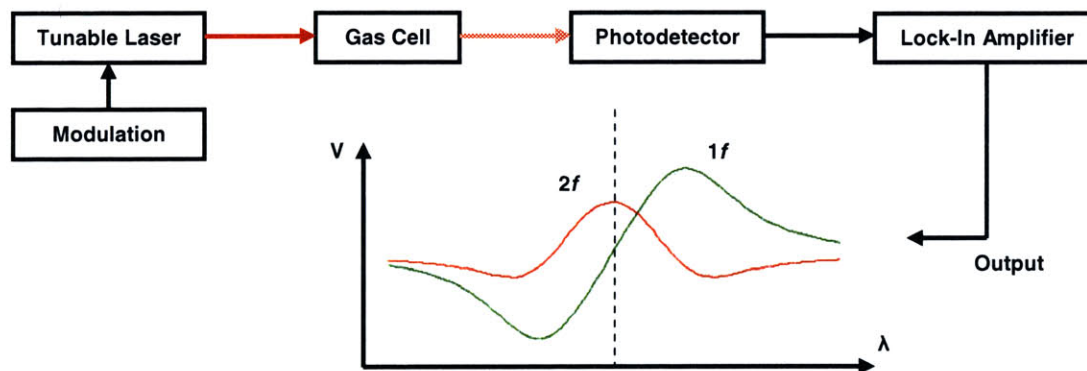
Figure 2-3 WMS system and characteristic $1f$ and $2f$ detection curves

2.3 Photoacoustic Spectroscopy (PAS)

Even higher detection sensitivities are achievable by exploiting the PA effect. Originally discovered by Alexander Graham Bell in 1880, the PA effect has reestablished its worth in the scientific community in recent times due to the development of advanced lasers [20]. It is central to a variety of emerging technologies such as photoacoustic tomography (PAT) [21, 22]

and versatile materials characterization techniques applicable to solids, liquids, or gases [23, 24]. Gas detection using the PA effect is actually a fairly old concept, but it remains one of the most sensitive methods known to date.

In PAS, light is converted into an acoustic signal via a nonradiative relaxation transition [20]. The acoustic signal is then picked up by a microphone. Typically, a modulated (AM or FM) laser beam is passed through the gas species to be interrogated. If the output wavelength of the laser matches an absorption wavelength of the gas, then optical energy is absorbed as dictated by the modulation and time-varying localized heating at the modulation frequency results from vibrational-rotational relaxation of the gas molecules [5]. In a gas cell of fixed volume, this time-varying heat generation produces pressure waves i.e. an acoustic signal at the same frequency. Using an acoustic sensor, the simplest of which is a commercial microphone, in combination with frequency-discriminating electronics e.g. lock-in amplifier, an electrical signal can be obtained whose strength is an indication of the concentration of the target gas in the gaseous mixture that is under examination. The experimental setup is illustrated in Figure 2-4.
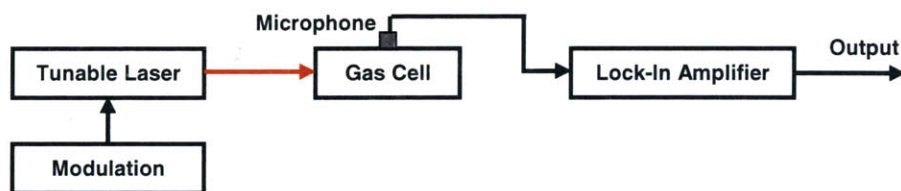
Figure 2-4 Experimental setup for PAS

There are essentially two key benefits of PAS relative to the other spectroscopic techniques covered in this chapter. First, only absorption of optical energy by gas molecules followed by acoustic signal generation through the PA effect can conceivably produce a sound signal at the chosen frequency [23]. Therefore, PAS directly measures the amount of absorption

of optical energy by the gas molecules. In contrast, conventional LAS measurements, as discussed in section 2.1.3, suffer from significant background signals. Second, the amplitude of the PA signal can be boosted by resonant Q-factor amplification if the laser modulation frequency corresponds to a resonance mode of the gas cell. It is fairly easy to design PA gas cells to provide 1-2 orders of magnitude amplification, and under certain circumstances it may be possible to achieve acoustic signal amplification by 3 orders of magnitude [25]. This boost in acoustic signal amplitude has been shown to improve the detection sensitivity past sub-ppb levels [26].

2.4 Hollow-Core Photonic Crystal Fiber (HC-PCF) Gas Sensing

Since its inception in 1991 and subsequent inaugural successful fabrication in 1995, photonic crystal fiber (PCF) has found itself at the forefront of science and technology [27]. The unique properties of PCFs, such as unprecedented control over dispersion characteristics and nonlinear interactions between light and gases, have rendered themselves useful for a wide variety of applications [27]. In particular, the advent of hollow-core fibers, not possible with standard step-index fibers, has opened up many possibilities in the world of laser spectroscopy [8]. These PCFs have air-guided cores that can be filled with gases which are then forced to interact with the light propagating through the optical fiber. The novel light confinement mechanism of PCFs is worth discussing, as it is quite different from that of conventional optical fibers.

2.4.1 Hollow-Core Photonic Crystal Fiber (HC-PCF)

Standard optical fibers rely on total internal reflection to keep light propagating in the core. The surrounding cladding has an index of refraction that is lower than that of the core, thus making it

possible for light to propagate down the length of the fiber exclusively in the core at specific entrance angles which are directly associated with a discrete set of modes [27]. In contrast, PCFs embrace the concept of photonic crystals to confine light propagation to the core of the fiber. Conceived by Eli Yablonovitch around 1987, photonic crystals are wavelength-scale periodic structures that refuse the propagation of light in all directions for a certain range of wavelengths also known as a photonic bandgap [27]. These photonic bandgaps are commonly observed in the colorful designs on butterfly wings, peacock feathers, and various holograms on credit cards [27]. Taking advantage of photonic bandgap guidance of light removes many of the limitations of step-index (total internal reflection) fibers, most importantly of which is the impossibility of having a hollow, air-filled core.
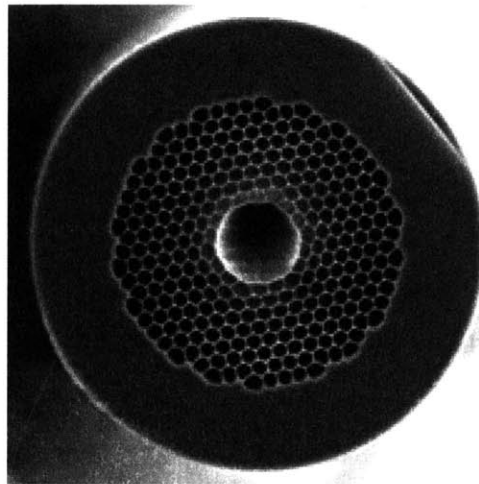
Figure 2-5 Cross-section of a HC-PCF featuring an air core, photonic crystal cladding [28]

A PCF is essentially a two-dimensional photonic crystal that has a defect at its center. A cross-section of a typical HC-PCF is illustrated in Figure 2-5. The 2D photonic crystal cladding consists of a periodic arrangement of air holes that run along the entire length of the fiber parallel to its axis. The photonic crystal is interrupted at the center by the core, which in Figure 2-5 is

hollow or air-filled. Light that is injected into the air core of the HC-PCF is then confined to travel down the core of the fiber, since it is unable to penetrate the photonic bandgap of the 2D photonic crystal that is the cladding. Currently, HC-PCFs are available commercially in wavelengths ranging from 400 nm to 2500 nm [8]. They are generally fabricated using a stack-and-draw technique where glass (fused silica) tubes are stacked together in a macro-sized preform, fused, and drawn down to fiber dimensions [27].

2.4.2 Application of HC-PCFs to Laser Spectroscopy

HC-PCFs present an intriguing capability. With their hollow cores, they are able to house gases and serve as gas cells. Also, as optical fibers, light from a laser is easily coupled into the core. These properties of HC-PCFs make them convenient, optically-accessible gas cells which are ideal for laser spectroscopy. Furthermore, they have been shown to maintain greater than 98% of the guided mode energy in the air-filled areas, mostly in the hollow core [8]. This feature ensures high interaction between the optical energy supplied by the laser source and the gas(es) in the gas cell, which is certain to improve the sensitivity of the spectroscopic approach. However, the most attractive quality of HC-PCFs with respect to laser spectroscopy is that they offer an easy means to implement long optical path lengths through which light can interact with the gas(es). Meters of fiber can be wound in a coil to fit in tight spaces. As discussed in section 2.1.2, long interaction lengths are a great help to the sensitivity of absorption-based laser spectroscopic techniques.

Filling a HC-PCF with a gas for research purposes is no trivial matter. Usually, the fiber is evacuated with a vacuum system and then promptly backfilled with the desired gas to the desired pressure. Experimentation can be done with the gas flow system intact, or the gas can be

sealed inside the PCF with fusion splices to standard single-mode optical fiber at both ends, thus preserving its optical accessibility. The latter option, so-called HC-PCF gas cells, is still an unperfected technology because splicing PCFs is difficult and in the time required for a good splice to be made, a considerable amount of the loaded gas can leak out by diffusion [29]. If accomplished successfully with minimal loss of gas, the sealing of HC-PCFs and the creation of novel gas cells can however provide the benefits of size, compactness, and ease of compatibility to standard fiber-based optical components [30]. These advantages are hard to realize while maintaining the gas flow vacuum system intact as part of the experimental setup.

Chapter 3

Theory

3.1 Classical PA Theory

The physics of PA signal generation and detection is covered thoroughly in a number of texts including [5]. In these texts, the process of PA signal generation is broken down into and analyzed in two steps. The first step encompasses the absorption of the modulated light by the gas molecules and the resulting production of heat with the same time variation. A rate-equation approach is used to model this step. The second step connects the generated heat to the acoustic signal that is ultimately detected by a microphone. This step is governed by a wave equation. If the sensitivity of the microphone is known, then the theory can be extended to approximate the amplitude of the PA detection signal.

3.1.1 Absorption of Light and Production of Heat

In PAS, a modulated laser beam is passed through a gas sample. The resulting absorption of the light by the gas and generation of heat via nonradiative vibrational-translational decay can be described by the rate equation for a simple two-level system. If N represents the density of absorbing gas molecules, n_1 the density of absorbing gas molecules in the excited state, $h\nu$ the energy of the transition between the upper (excited) state and the lower state, $\Delta\nu$ the linewidth, S the associated line strength (m/molecule), τ_R the radiative lifetime, τ_C the collisional decay time,

and $I(t) = I_0[1 + f(t)]$ the modulated intensity of the light at frequency specified by $f(t)$, then the upper state population is sufficiently described by [5]:

$$\frac{dn_1}{dt} = -n_1\left[\frac{I}{h\nu}\left(\frac{S}{\pi\Delta\nu}\right) + \tau_C^{-1} + \tau_R^{-1}\right] + (N - n_1)\left(\frac{I}{h\nu}\right)\left(\frac{S}{\pi\Delta\nu}\right) \tag{3-1}$$

Collisional excitation of the upper state is omitted from (3-1), a safe assumption given that $h\nu \gg kT$ where k is Boltzmann's constant and T is the temperature of the gas. If the modulation of the light, represented by $f(t)$, is slow enough, then the system can be approximated as quasi-static and the solution to (3-1) is given by [5]:

$$\frac{n_1}{N} = \frac{(IS / h\nu\pi\Delta\nu)}{(2IS / h\nu\pi\Delta\nu) + \tau^{-1}} \tag{3-2}$$

where $\tau^{-1} = \tau_R^{-1} + \tau_C^{-1}$. (3-2) can be simplified in the case of two limits: the case of transition saturation where I is large and $2IS/h\nu\pi\Delta\nu \gg \tau^{-1}$ and the case of small I where $2IS/h\nu\pi\Delta\nu \ll \tau^{-1}$. If the intensity of the light is strong enough to saturate the transition, then the absorbing gas molecules will be equally split between the upper and lower states, or

$$\frac{n_1}{N} = \frac{1}{2} \tag{3-3}$$

On the other hand, if the light intensity is weak enough, then [5]

$$\frac{n_1}{N} = \frac{IS\tau}{h\nu\pi\Delta\nu} \tag{3-4}$$

This result is significant in that under the conditions of adequately slowly-varying and weak light intensity I, the upper state population n_1 is directly proportional to I. Heat is produced by collision-induced nonradiative relaxation of the excited gas molecules in the upper state at a rate determined by the upper state population, collisional decay time, and energy of the transition according to [5]:

27

$$H = \left(n_1 \, / \, \tau_C\right)h\nu \tag{3-5}$$

where H represents the rate of heat generation (W/m^3). Since radiative relaxation times are typically several orders of magnitude longer than nonradiative decay times, especially in the NIR or IR where radiative decay times are somewhere between 10^{-1}s and 10^{-3}s and nonradiative relaxation times for vibrational-translational decay are in the area of 10^{-9}s [20],

$$\tau \approx \tau_C \tag{3-6}$$

Therefore, (3-5) can be rewritten using (3-4):

$$H = \frac{NS}{\pi\Delta\nu}I \tag{3-7}$$

Clearly, the rate of heat generation is simply related to the intensity of the light incident upon the gas molecules if it is sufficiently slowly varying and weak. (3-7) has the form of

$$H = \alpha I \tag{3-8}$$

where the absorption coefficient or absorbance α representing the energy conversion from light into heat is given by [5]

$$\alpha = \frac{NS}{\pi\Delta\nu} \tag{3-9}$$

To provide a more concrete idea of what the slowly-varying and weak criteria for the intensity of the light actually indicate for a real implementable PA system, typical numbers can be used to calculate approximate design limits. For example, the sufficiently weak criterion can be written with the help of (3-9)

$$I_0 << \frac{h\nu N}{2\alpha\tau_C} \tag{3-10}$$

For propane or methane at 3.392 µm, (3-10) suggests that the upper limit for the light intensity is around 10^{13} W/m^2 [31]. For acetylene at 1.532 µm, the upper limit is even higher due to a

smaller α in the NIR. If the output power of the laser source is on the order of 1 mW, then the minimum cell radius for the PA gas cell is on the order of nanometers.

Similarly, the slowly-varying requirement can be expressed as [5]

$$\omega << \frac{2I_0\alpha}{h\nu N} + \tau^{-1} \qquad (3\text{-}11)$$

if the modulation of the light is sinusoidal and ω is the angular frequency of the modulation. Holding the condition of (3-6) to be true and assuming that the sufficiently weak criterion of (3-10) is met, it can be shown that (3-11) simplifies to:

$$\omega << \frac{1}{\tau_c} \qquad (3\text{-}12)$$

If the collisional decay time is approximated to be 10^{-9} s, then (3-12) yields an upper bound of ω $<< 10^9$. This means that the modulation frequency cannot exceed 160 MHz. There is also a lower limit to the modulation frequency imposed by the thermal diffusion of heat into the walls of the PA gas cell containing the absorbing gas species. If the modulation frequency is too slow such that heat energy is allowed to diffuse away, then the dynamics of the acoustic signal generation process will be altered as (3-8) no longer holds. Typically, thermal diffusion times are on the order of 0.1s, meaning that PA modulation frequencies should exceed several Hz [20].

3.1.2 Acoustic Signal Generation

If the modulation of the light being absorbed by the gas molecules is slow enough and the intensity of the light is weak enough so that the absorbing transition is not saturated, then heat is generated according to (3-8) at a rate that varies directly proportional to the time-varying light intensity. What remains to be seen is how the production of heat relates to acoustic signal generation. This connection can be made through the inhomogeneous wave equation [20]:

$$\nabla^2 p - \frac{1}{c^2}\frac{\partial^2 p}{\partial t^2} = -\frac{\gamma-1}{c^2}\frac{\partial H}{\partial t} \qquad (3\text{-}13)$$

where $p(r,t)$ is the acoustic pressure, c is the speed of sound in the gas, γ is the specific heat ratio for the gas, and $H(r,t)$ is the rate of heat generation consistent with (3-5)-(3-8). In (3-13), terms accounting for losses due to heat conduction and viscosity have been omitted, simplifying the analysis which will remain adequate for most PA applications [5]. The solution to the inhomogeneous wave equation can be determined by first taking the Fourier transform and solving for the normal mode solutions of the homogeneous wave equation. The Fourier transform of (3-13) is given by [5]:

$$\left(\nabla^2 + \frac{\omega^2}{c^2}\right)p(r,\omega) = \left[\frac{\gamma-1}{c^2}\right]j\omega H(r,\omega) \qquad (3\text{-}14)$$

Traditionally, the walls of a PA cell are considered rigid and the condition of vanishing normal acoustic velocity at the walls gives rise to the homogeneous wave equation

$$\left(\nabla^2 + \frac{\omega_k^2}{c^2}\right)p_k(r) = 0 \qquad (3\text{-}15)$$

where p_k represents the normal modes and ω_k represents the associated resonance frequencies at which the modes are excited [20]. For a cylindrical gas cell of radius R and length L, the normal mode solutions have been shown to be of the form:

$$p_k = J_m(k_r r)\cos(k_z z)\frac{\sin}{\cos}(m\phi) \qquad (3\text{-}16)$$

where r, φ, and z are the cylindrical coordinates, J_m is the mth-order Bessel function of the first kind, and the wavenumbers k_r and k_z obey

$$\frac{\omega_k}{c} = \sqrt{k_r^2 + k_z^2 + \frac{m^2}{R^2}} \qquad (3\text{-}17)$$

30

and are given by [5]:

$$k_r = \frac{\pi \alpha_{mn}}{R}$$ (3-18)

$$k_z = \frac{\pi n_z}{L}$$ (3-19)

The indices $n = 0, 1, 2..., m = 0, 1, 2..., n_z = 0, 1, 2...$ correspond to the radial, azimuthal, and longitudinal mode contributions to a particular mode specified by (n,m,n_z) as shown in Figure 3-1, and α_{mn} is the nth root of the equation

$$\frac{dJ_m}{dr}\Big|_{r=R} = 0$$ (3-20)
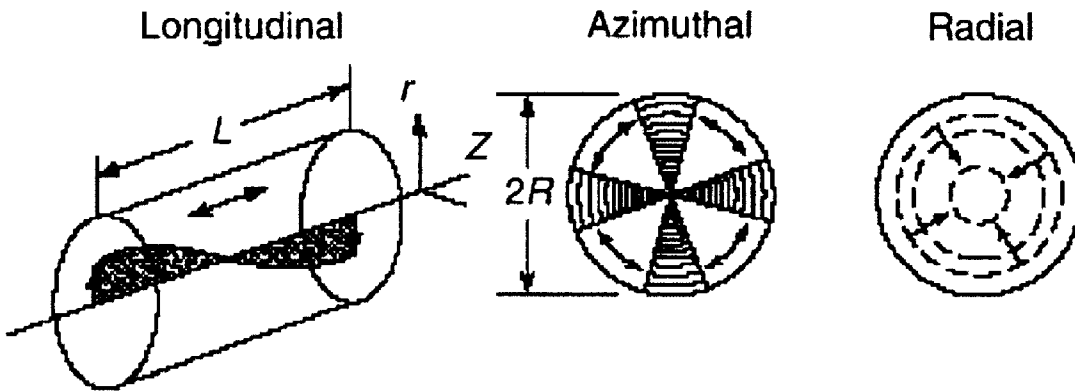
Figure 3-1 Acoustic resonance modes for cylindrical resonator [32]

In most cases, laser excitation is introduced in a direction parallel to the axis of the cylindrical gas cell, which does not excite any azimuthal modes ($m = 0$) and preferentially excites radial modes over longitudinal ones [20]. Using (3-17)-(3-20), the normal mode frequencies can be calculated for any mode (n,m,n_z) e.g. the lowest-order radial mode (1,0,0) or longitudinal mode (0,0,1) [5].

From the normal mode solutions $p_k(r)$, the acoustic pressure $p(r,\omega)$ can be written as the following summation [5]:

$$p(r,\omega) = \sum_k A_k(\omega)p_k(\omega) \tag{3-21}$$

where $A_k(\omega)$ is the mode amplitude for each normal mode $p_k(\omega)$. Substituting (3-21) into (3-14) and utilizing the property that the modes p_k are orthogonal, it can be derived for the mode amplitude [20]:

$$A_k(\omega) = -\frac{j\omega(\gamma-1)}{\omega_k^2 - \omega^2 - j\omega\omega_k/Q_k}\frac{1}{V}\int_V p_k^* H dV \tag{3-22}$$

where Q_k is the resonance quality factor that takes into account damping effects and V is the volume of the PA gas cell. From (3-22), the advantage of resonant PAS can be seen. The mode amplitude for nonresonant excitation i.e. the zero-order mode ($\omega_0 = 0$), assuming that the conditions are satisfied for (3-8) to be true, the absorption of light along the cylindrical axis of the gas cell is negligible for trace gas concentrations, and the laser beam intensity is spatially constant, can be shown to be

$$A_0(\omega) = -\frac{j\alpha(\gamma-1)PL}{\omega(1 - j/\omega\tau_0)V} \tag{3-23}$$

where $\tau_0 = Q_0/\omega_0$ is the damping time of the zero-order mode resulting from the conduction of heat from the gas to the walls of the enclosing gas cell and the light intensity I is expressed in terms of the power P as PL/V [20]. On the other hand, the mode amplitude for resonant excitation of a first-order mode is given by

$$A_1(\omega) = -\frac{j\omega\alpha(\gamma-1)PL}{(\omega_1^2 - \omega^2 - j\omega\omega_1/Q_1)V} \tag{3-24}$$

Comparison of resonant to nonresonant PA operation can be made by analyzing (3-23) and (3-24). At very low frequencies, $\omega\tau_0 \ll 1$ and A_0 is approximately constant with value $\alpha(\gamma$-

1)$PL\tau_0/V$. In contrast, the first-order mode is far from its resonance frequency i.e. $\omega \ll \omega_1$ so A_1 is very small. At higher frequencies where $\omega\tau_0 \gg 1$, the mode amplitude of the zero-order mode decreases as ω increases. As ω approaches ω_1, A_1 eclipses A_0 and hits its maximum value of $\alpha(\gamma-1)PLQ_1/\omega_1V$. Therefore, although nonresonant operation is viable at low frequencies (several Hz), it is preferable to excite a resonant mode at its resonance frequency and reap the benefits of quality factor amplification of the acoustic signal amplitude and decreased noise from moving to higher frequencies. This improved signal-to-noise ratio is central to the attractiveness of PAS for high sensitivity gas detection.

3.1.3 Acoustic Signal Detection

To be complete, a geometrical factor G is added to (3-24) to account for the radial dependence of the laser beam power such that for resonant excitation of the first-order mode, the resulting acoustic signal amplitude is given by [5]

$$p_1(r,\omega) = A_1(\omega_1)p_1(r) = \frac{\alpha(\gamma-1)GPLQ_1}{\omega_1V}p_1(r) \tag{3-25}$$

In general, $G \approx 1$ for typical laser beam profiles [20]. The acoustic signal is traditionally detected by a microphone which produces a voltage signal output related to the acoustic signal amplitude by its sensitivity R_{mic}. R_{mic} has units of volts per unit pressure and is usually on the order of mV/Pa [20]. Theoretically, the amplitude of the voltage signal output is the product of the acoustic signal amplitude and the detection sensitivity of the microphone, or

$$S = \frac{\alpha(\gamma-1)GPLQ_1}{\omega_1V}R_{mic}p_1(r_{mic}) \tag{3-26}$$

where S represents the voltage output signal amplitude and r_{mic} is the location of the microphone in the PA gas cell [20]. For conceptual simplicity, (3-26) is occasionally written as

33

$$S = C\alpha P \tag{3-27}$$

where the cell constant C (Vm/W) is given by

$$C = \frac{(\gamma - 1)GLQ_1}{\omega_1 V} R_{mic} p_1(r_{mic}) \tag{3-28}$$

and represents the conversion from optical power to electrical output signal for the PA system [20]. In most cases, the cell constant C can be determined experimentally using a gas whose absorption coefficient is known and a laser source whose output power has been measured. It is a characteristic measurement of the detection sensitivity of the PA system in that the larger the cell constant, the more sensitive the system is. In other words, if one PA system generates a larger output voltage signal than another one, holding all the parameters e.g. laser output power, gas identity, concentration, and absorption cross-section to be the same for both systems, then the one with the larger cell constant is the more sensitive system.

Clearly, from (3-28) it is apparent that higher detection sensitivity for a PA system is dependent on two parameters. First, V/L is simply the cross-sectional area of the gas cell, or πR^2 for a cylindrical gas cell of radius R. As a result, the cell constant C and also the detection sensitivity are inversely proportional to the cross-sectional area, meaning that gas cells with smaller radii are favorable for higher sensitivity. Second, the cell constant is also inversely related to ω_1/Q_1 which is equal to the resonance linewidth $\Delta\omega_1$ by definition of the resonance quality factor. Thus, narrow resonances lead to higher detection sensitivities although a practical limit of several Hz is imposed by the difficulty of staying locked to a resonance frequency ω_1 which varies fairly sensitively with environmental conditions [20]. These two dependencies of the detection sensitivity on cell radius and resonance width are the primary reasons why the possibility of using a HC-PCF as a resonant PA gas cell is an intriguing idea to achieve high sensitivity detection. The latter will be explained in the next section.

34

3.2 HC-PCF as PA Cell

Conceptually, the simplicity of utilizing HC-PCF as a gas cell for resonant photoacoustics is greeted with a number of challenges. First, the size and structure of HC-PCF makes it impossible to use commercial transducers for the detection of the PA signal as is done in conventional PAS. Even the smallest available transducers cannot fit into the 10-20μm cores of HC-PCFs, nor can a HC-PCF be opened up to allow access to an acoustic signal in the core. One idea is to maintain the convenience of using commercial transducers for acoustic signal detection by taking advantage of the unique resonance properties of fused silica. If instead of behaving as a rigid acoustic resonator for the PA signal (i.e. the gas resonates) the HC-PCF structure is driven by the PA signal at a mechanical resonance frequency of a pure radial mode, then a measurable acoustic signal can be found at the surface of the fiber. By placing a commercial transducer flush against or close to the surface of the fiber, the acoustic signal can be detected. To evaluate this idea, PA theory will be revisited. From (3-28), there are three key parameters of HC-PCF to investigate to effectively assess the merits of this approach: the air-core (gas cell) radius, the mechanical resonance frequency of the HC-PCF structure, and the associated quality factor of that resonance. Obviously, the tiny size of the HC-PCF core is highly advantageous as the PA signal is anticipated to be inversely related to the cross-sectional area of the PA cell. However, the resonance characteristics of HC-PCF must be examined before any conclusion can be drawn on the idea of using HC-PCF as a PA cell.

3.2.1 Mechanical Resonance Frequency of HC-PCF

Due to the complicated nature of the mathematics governing hollow cylinders, nevermind the extreme complex structure of HC-PCFs, finite element simulation is required to determine the

vibrational resonance frequencies. To estimate the frequency of the first pure radial mode of a HC-PCF, ANSYS Workbench was used. The simulated structure was created in SolidWorks, adhering to the physical specifications provided by Blaze Photonics, the manufacturer of 1550 nm HC-PCFs. To avoid outrageous simulation times on the order of weeks, a very thin slice of fiber of length 10 μm was simulated rather than an entire length of fiber of several meters. Since pure radial modes are by nature largely independent of fiber length [33], it was assumed that the calculated results of the simulation would be sufficient in accuracy to represent those for a HC-PCF of much greater length. Figure 3-2 shows the SEM image of the cross-section of the HC-PCF from the datasheet along with the recreated cross-section of the eventual simulated structure.

(a)

(b)
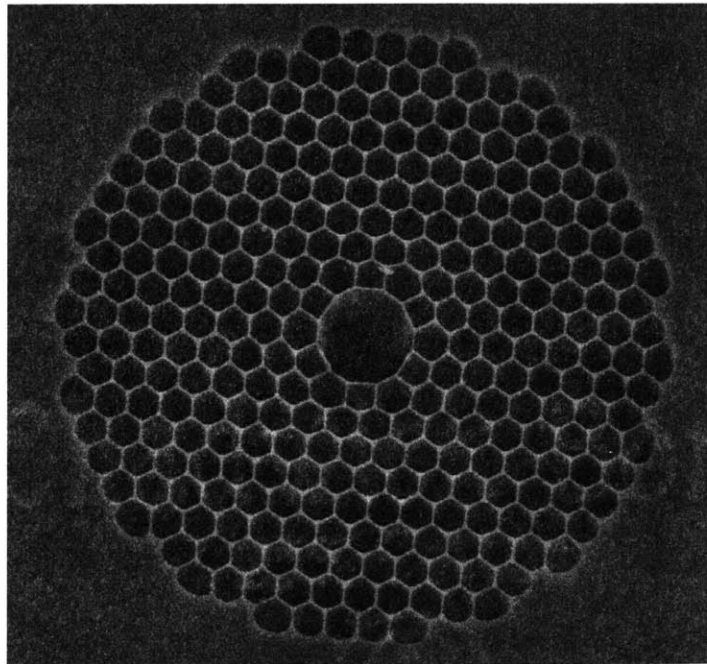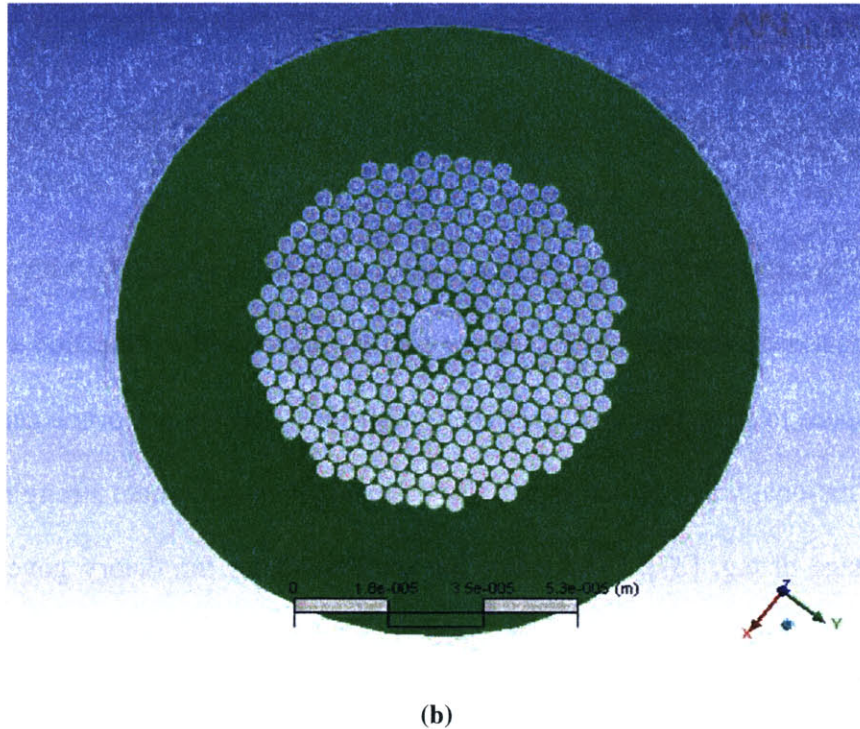
Figure 3-2 (a) SEM photograph of HC-PCF cross-section [34] and (b) model of HC-PCF structure for

ANSYS simulation

The core diameter of the HC-PCF was 11 μm, the diameter of the holey region was 70 μm, the diameter of the entire cladding was 120 μm, and the pitch or distance between cladding hole centers was 3.8 μm. Although the actual cladding holes were hexagonal in shape, they were modeled as circular holes for the sake of simplicity while maintaining an air filling fraction greater than 90%. Under the condition of free vibration, the resonance frequencies of the fused silica HC-PCF were determined with the ANSYS Workbench Frequency Finder. The first pure radial mode occurred at roughly 8 MHz.

3.2.2 Resonance Quality Factors of Fused Silica Fibers

HC-PCFs are made out of fused silica, a material with unique mechanical resonance properties. Recently, there has been great interest in studying these resonance characteristics for the advancement of gravitational wave detectors which require components with extremely low internal loss to minimize thermal noise, the key limiting factor of the detection sensitivity [35]. Fused silica happens to have very low internal friction [36], making it a prime candidate for use not only in gravitational wave detectors but also other applications where strong resonances can be taken advantage of e.g. [37]. The following sections detail the theory governing the high resonance quality factors of fused silica cylinders. The main sources of vibrational damping will be identified and discussed with respect to fused silica cylinders of comparable size to HC-PCFs.

3.2.2.1 Thermoelastic Damping

Thermoelastic losses arise from the flow of local heat currents that originate from stress inhomogeneities in a vibrating structure [38]. The loss angle $\varphi_{th} = Q_{th}^{-1}$ associated with thermoelastic loss in a solid cylinder of diameter d is given by

$$\phi_{th}(f) = \frac{Y\alpha^2 T}{C} \frac{\eta f}{1 + \eta^2 f^2}$$

(3-29)

where f is the frequency of vibration and the material parameters Y, α, T, and C are the Young's modulus (Pa), thermal expansion coefficient (K^{-1}), temperature (K), and heat capacity per unit volume (J/K•m^3) of the material the cylinder is made out of e.g. fused silica [39]. The parameter η has units of seconds and is given by

$$\eta = \frac{2\pi}{13.55} \frac{Cd^2}{\kappa}$$

(3-30)

where κ represents the thermal conductivity (W/m•K) of the material [39]. There are several notable observations that can be made from (3-29). First, the thermoelastic loss is frequency dependent, and will exhibit a peak at a frequency $f_{peak} = \eta^{-1}$. If $f \ll \eta^{-1}$, then φ_{th} varies directly with f. On the other hand, if $f \gg \eta^{-1}$, then the thermoelastic loss is inversely proportional to the vibrational frequency. For fused silica, $Y \approx 73$ GPa, $\alpha \approx 0.55$ μ/K, the specific heat capacity $C_m \approx$ 740 J/kg•K, the mass density $\rho \approx 2200$ kg/m^3, and $\kappa \approx 1.38$ W/m•K. Assuming $T = 300$K and evaluating $C = \rho C_m$, the thermoelastic loss for a fused silica cylinder of diameter $d = 125$ μm, roughly the size of HC-PCFs, is governed by $\eta = 0.0085$ s and

$$\phi_{th}(f) \approx 4 \times 10^{-6} \frac{\eta f}{1 + \eta^2 f^2} \tag{3-31}$$

If $f \ll \eta^{-1} = 117.65$ Hz, then $\varphi_{th} \approx 3.4 \cdot 10^{-8} f$. However, the vibrational resonance frequencies of a cylinder of that size are much higher than η^{-1} [33], meaning that $\varphi_{th} \approx 4.7 \cdot 10^{-4}/f$ or $Q_{th} \approx 2125 \cdot f$.

3.2.2.2 Bulk and Surface Losses

Energy dissipation due to internal friction results in losses in the bulk material as well as the surface layer of any vibrating body [39]. In general, the total loss angle contribution for internal friction can be expressed:

$$\phi_{int} = \phi_{bulk} + \phi_{surf} \tag{3-32}$$

where the surface loss term is related to the bulk loss term by

$$\phi_{surf} = \phi_{bulk} \left(\mu \frac{d_s}{V / S} \right) \tag{3-33}$$

In (3-33), μ is a constant that takes into account the shape of the vibrating structure and the type of resonance mode being excited, d_s is the dissipation depth (m) which characterizes the relative strength of energy dissipation in the surface layer compared to the bulk, and V/S is the volume-

39

to-surface area ratio [35]. Empirical evidence has shown that the surface loss dominates the bulk loss when the diameter of fused silica solid cylinders falls below several millimeters [40]. Therefore, for a fused silica cylinder of HC-PCF size,

$$\phi_{int} \approx \phi_{surf} \tag{3-34}$$

Unlike the bulk loss, the surface loss for fused silica has been established to be frequency independent [39]. Consequently, the surface loss can be considered as

$$\phi_{surf} = \mu\alpha_{surf}\frac{S}{V} \tag{3-35}$$

where α_{surf} is a frequency-independent parameter with units of length. For cylindrical geometry, $S/V = 4/d$ and the constant $\mu = 2$ for transverse modes. The surface loss parameter α_{surf} depends critically on the manufacturing process and polishing used for the fused silica, and also on the condition of the surface [35]. The value of α_{surf} can be as small as a few picometers for flame-drawn or flame-polished fused silica, but can be much bigger if damage in the form of microcracks is present at the surface [35]. From (3-35), a lower limit of $\varphi_{surf} \approx 6.4 \bullet 10^{-8}$ can be estimated for a fused silica rod of similar diameter $d = 125\mu m$ to a HC-PCF.

3.2.2.3 Residual Gas Damping

Thus far, intrinsic sources of damping have been covered. In most cases, measures can be taken to effectively eliminate any extrinsic sources of damping from the experimental setup. However, a vibrating body outside of a vacuum will experience damping from the surrounding air or other composition of gases. Depending on the circumstances, the damping from the ambient gas may be so large that intrinsic damping effects cannot be observed. The loss angle for gas damping is given by

40

$$\phi_{gas} = \frac{\bar{v}}{\pi f d} \frac{\rho_{gas}}{\rho_{cylinder}} \qquad (3\text{-}36)$$

where $\bar{v}$ is the average speed (m/s) of the gas molecules, and ρ_{gas} and $\rho_{cylinder}$ are the mass densities (kg/m^3) of the gas and the resonating cylinder material respectively [39]. The average speed of gas molecules can be determined by equating the average kinetic energy to the thermal energy for an individual molecule:

$$\frac{1}{2} m \bar{v}^2 = \frac{3}{2} kT \qquad (3\text{-}37)$$

where $\bar{m}$ is the average mass of the molecule, k is Boltzmann's constant, and T is the temperature in Kelvin. As an example, the average speed of air molecules ($M = 28.97$) at room temperature is approximately 508 m/s. Therefore, assuming atmospheric pressure with $\rho_{air} = 1.17$ kg/m^3 and $\rho_{silica} = 2200$ kg/m^3,

$$\phi_{gas} \approx \frac{688}{f} \qquad (3\text{-}38)$$

for a fused silica rod with a diameter of 125μm.

3.2.2.4 Application to HC-PCFs

Clearly, the analysis of 3.2.2.1-3.2.2.3 merely identifies the three major sources of damping for a resonant vibrating fused silica solid cylinder and presents how they compare when the dimensions shrink to optical fiber size. What has yet to be addressed is how the analysis applies to a complicated structure like a HC-PCF. The reality is such a connection is difficult to make without large assumptions. Even progressing from a solid cylinder to a hollow cylinder geometry, there is much doubt as to the validity of using governing equations of the former case

41

to analyze the latter. What can be done is estimate the resonance quality factor for a solid fused silica cylinder of size comparable to HC-PCF. This calculation establishes an extreme upper limit for the quality factor of a HC-PCF structure, since there would be additional damping caused by the gas in the core and the holes running parallel to it that would be absent from a solid cylinder structure.

The total loss is the sum of the losses due to thermoelastic damping, surface loss damping, and gas damping:

$$\phi_{tot} = \phi_{th} + \phi_{surf} + \phi_{gas} \tag{3-39}$$

The resonance quality factor $Q = \varphi_{tot}^{-1}$ can be expressed in terms of the resonance frequency f for a solid fused silica cylinder of diameter $d = 125$ μm from (3-31), (3-35), and (3-36):

$$Q = \cfrac{1}{\cfrac{4.7 \times 10^{-4}}{f} + 6.4 \times 10^{-8} + \cfrac{688}{f}} \tag{3-40}$$

From section 3.2.1, the first pure radial mode frequency was determined to be 8 MHz. Substituting this value into (3-40), it can be determined that

$$Q_{max} \approx 1.162 \times 10^4 \tag{3-41}$$

3.3 Analysis of PA Signal using HC-PCF as PA Cell

Assuming that the dependencies of the PA signal on the gas cell size, resonance frequency, and quality factor in a HC-PCF are the same as for a rigid cell, then the amplitude of the PA signal for a kth-order resonant mode follows

$$A_k\left(\omega_k\right) \propto \frac{Q_k}{\omega_k d^2} \tag{3-42}$$

where the quality factor is of the mechanical resonance of the fiber. For most PA systems, light excitation is provided down the axis of the gas cell, and the resulting acoustic signal is radial in nature. Consequently, the PA signal exerts pressure on the walls and if it is strong enough and the frequency is proper, it can excite a pure radial mode of the HC-PCF. From section 3.2, it is apparent that resonance linewidths (ω/Q) on the order of kHz can be expected for HC-PCF. While these linewidths are 1-2 orders of magnitude larger than those reported for conventional PAS, ultimately the product of the resonance linewidth and the cross-sectional area of the HC-PCF is much smaller than for conventional PA gas cells. Since the amplitude of the PA signal is inversely proportional to this product, it would indicate that utilizing HC-PCF for PAS as a novel PA cell would lead to improved detection sensitivity.

The amplitude of the PA signal generated with a HC-PCF gas cell can be estimated for the detection of C_2H_2 gas at 200 Torr using (3-26). Assuming that G and $p_1(r)$ are on the order of unity, and α is approximated to be 0.6 cm^{-1}, $\gamma = 1.237$ for C_2H_2, P is estimated to be 1 mW, and the resonance linewidth ω/Q is estimated by the results of section 3.2, then the amplitude of the acoustic signal is approximately 7.655 kPa. However, this signal amplitude could drop by several orders of magnitude due to coupling inefficiencies between the HC-PCF and the chosen transducer. Still, considering that typical sensitivities for commercial microphones are on the order of tens of mV/Pa and the fact that lock-in amplifiers are capable of measuring signals with amplitudes down to the nV range, there should not be any difficulty in detecting the PA signal using a standard ultrasonic transducer.

Chapter 4

Laser Wavelength Stabilization

An exercise was performed to gain familiarity with a widely used laser wavelength stabilization technique. The goal of the exercise was to successfully lock the output wavelength of a distributed feedback (DFB) diode laser to an absorption peak wavelength of acetylene (C_2H_2) in the near infrared (NIR) spectrum. Acetylene was chosen because of its strong NIR absorption features, particularly in the vicinity of the nominal output wavelength of the DFB diode laser (1532 nm), and commercial availability in the form of tiny fiber-coupled gas cells, which are extremely convenient for optical setups. This chapter is divided into two main sections. The first section presents an overview of the laser wavelength stabilization techniques that were considered, along with the basic theory of the method that was chosen. In the second section, data relevant to the process of implementing the laser wavelength stabilization system is presented. The section concludes with proof of the effectiveness of the actual system that was put together.

4.1 Laser Wavelength Stabilization Techniques

4.1.1 Side locking vs. Peak Locking

There exist a number of methods to stabilize the wavelength of a laser by eliminating drift and fluctuations in the laser output. In particular, locking the output wavelength of a diode laser to an absorption line used as an external wavelength reference is a common practice that can be

accomplished in one of two ways. The wavelength can either be locked to a point on the side of the absorption line profile (side locking) or to the line center or peak (peak locking). Both techniques take advantage of feedback to correct for deviations in the diode laser output wavelength away from the target locking point wavelength. Typically, a feedback error signal is generated using the absorption line, and serves to adjust the laser current such that the output wavelength is restored back to the locking point wavelength. Current is preferred over temperature as the adjustable control parameter for feedback compensation because current is capable of responding quickly to changes whereas temperature is not. The generic setup of such a wavelength stabilizing system is depicted in Figure 3-1. At the target locking point wavelength, the feedback error signal is 0. If the laser output wavelength increases, a negative error signal is generated to decrease the laser current and push the output wavelength back to the locking point wavelength. Likewise, if the wavelength decreases, a positive error signal is produced to restore it to its locking point value.
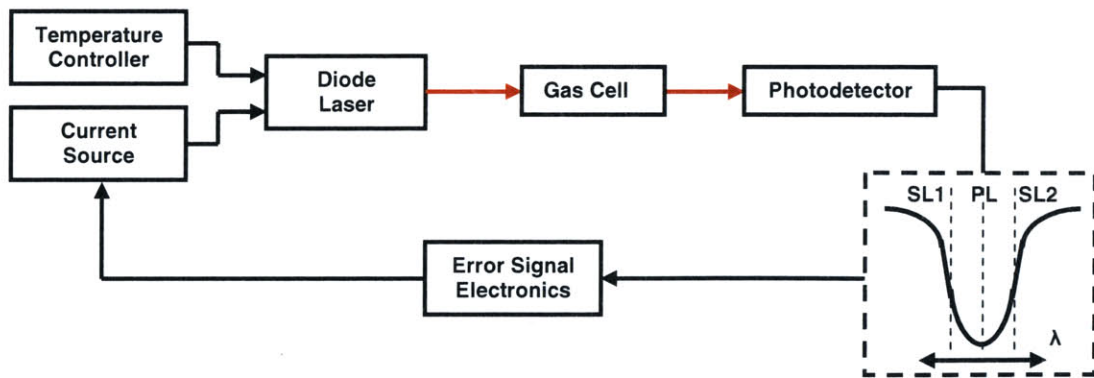

Figure 4-1 Concept of diode laser wavelength stabilization to an atomic absorption line

Side locking and peak locking require different electronics to generate an error signal with the proper characteristics. In side locking, the output wavelength of the diode laser is

locked to either of the points of maximum slope on the reference absorption line (designated by SL1 and SL2 in Figure 4-1). The difference between the photodetector output signal and a reference voltage equal to the output voltage of the photodetector at either of the side locking points would be taken with a differential amplifier to produce the error signal. For the case of locking the laser wavelength to the point labeled SL2 in Figure 4-1, the photodetector output would be subtracted from the reference voltage. Precisely at SL2, the difference error signal would be 0 V. If the wavelength of the diode laser increases, the photodetector output signal increases, the error signal becomes negative, and feeding it into the external modulation input of the current source causes the current, and subsequently the laser output wavelength, to decrease until the error signal is 0 V i.e. the wavelength is restored to that at SL2. On the other hand, if the wavelength of the diode laser decreases, the photodetector output signal decreases, the error signal is positive, and the result of the feedback is a similar restoration of the wavelength to SL2. For the case of locking the laser wavelength to SL1, the reference voltage would instead be subtracted from the photodetector output signal and the signs of the error signal would be opposite of those for the case of locking to SL2, but the wavelength stabilization principle remains the same.
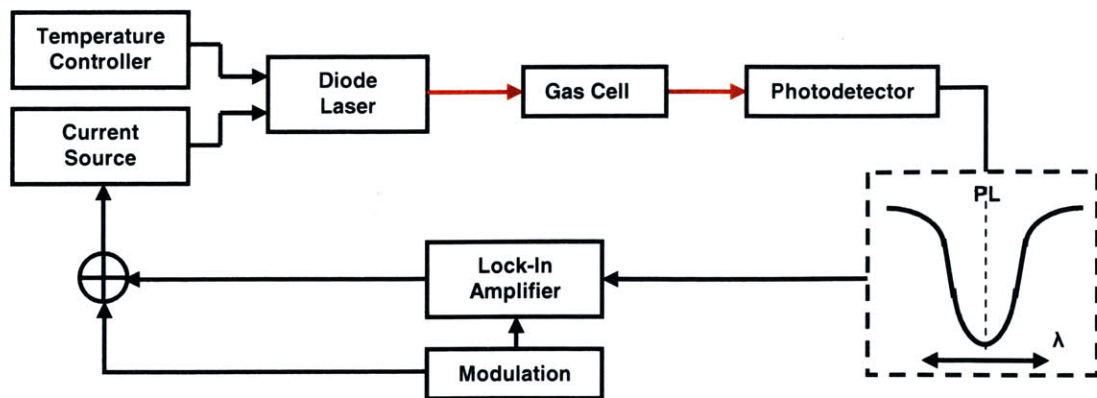

Figure 4-2 Concept of peak locking diode laser wavelength stabilization

Peak locking to the absorption line center (labeled PL in Figure 4-1) demands a more complicated method of stabilizing the diode laser output wavelength due to the symmetry of the absorption lineshape about the line center wavelength. It requires that the wavelength be modulated, which can be achieved by modulating the laser current (not shown in Figure 4-1). A more detailed diagram of a peak locking system is provided in Figure 4-2. A sinusoidal voltage signal can be introduced through the external modulation input of the current source to superimpose the desired current modulation on the bias current, resulting in wavelength modulation about the wavelength corresponding to the bias current. The error signal for peak locking is produced by a lock-in amplifier which is configured to measure the phase-sensitive amplitude of an input signal component at the modulation frequency i.e. $1f$ or 1st harmonic detection. Assuming that the sine signal used to dither the laser current about the bias current set by the current source also serves as the reference signal for the lock-in amplifier and the output of the photodetector is sent to the input of the lock-in amplifier, the error signal is 0 at the peak absorption wavelength. The photodetector output at the absorption line center wavelength undergoes two maxima for every maximum of the reference modulation signal. Therefore, it theoretically consists purely of a signal at twice the modulation signal frequency ($2f$), and the $1f$ signal component amplitude measured by the lock-in amplifier is 0. If the operating point wavelength strays from the absorption line center wavelength, the $2f$ signal component amplitude decreases and the $1f$ signal component amplitude increases. The sign of the $1f$ signal detected by the lock-in amplifier when the wavelength increases is positive because the variations in the photodetector output are in phase with the reference modulation signal. When the wavelength decreases, the output signal of the photodetector is completely out of phase with the reference modulation signal and the sign of the $1f$ signal detected by the lock-in amplifier is negative.

Clearly, sign inversion of the lock-in amplifier signal is required in order for the error signal to exhibit the right characteristics for feedback compensation of the current source bias current. The addition of sign inversion is rather trivial and can be implemented in a number of ways, including shifting the phase of the lock-in amplifier reference signal by 180°. The concept of error signal generation for peak locking is very similar to the principle behind wavelength modulation spectroscopy.

In general, peak locking is a superior technique relative to side locking. The major drawback of side locking is that the locking point is susceptible to fluctuations in the diode laser output power resulting from alignment instabilities. Any changes in the laser power would be interpreted by the system in Figure 4-1 to be caused by deviations of the laser wavelength from the locking point wavelength, and the subsequent correction of the bias current would erroneously shift the locking point. Ultimately, long-term drifts in the diode laser output wavelength are likely to occur. Peak locking, on the other hand, is less vulnerable to non-current related fluctuations in the laser output power. For this reason and other considerations associated with the intended direction of the research, it was chosen to stabilize the diode laser output wavelength by peak locking to an absorption line of C_2H_2 near 1532 nm.

4.1.2 Theory of Peak Locking

The error signal for side locking is odd-symmetric and linear as a function of wavelength about either of the points of maximum slope on the absorption lineshape. For peak locking, the error signal is also odd-symmetric, but has a more complicated shape. Fortunately, simple mathematics is sufficient to determine the theoretical shape of the error signal as a function of wavelength. Assuming that the reference absorption line is pressure-broadened, the output of the

photodetector in Figure 4-2 i.e. the transmitted light has the form of an inverted Lorentzian function with respect to wavelength $A_{pd}(\lambda)$:

$$A_{pd}(\lambda) = C_1 - C_0 \frac{2\alpha}{\alpha^2 + (\lambda - \lambda_0)^2} \tag{4-1}$$

where λ is the wavelength, λ_0 is the absorption line center wavelength, α is a parameter related to the width of the absorption line, C_0 is a normalization constant, and C_1 represents the photodetector output off the absorption line. If the laser wavelength is modulated, then (4-1) can be modified to:

$$A_{pd}(\lambda) = C_1 - C_0 \frac{2\alpha}{\alpha^2 + (\lambda + C_3 \sin(\omega_{mod} t) - \lambda_0)^2} \tag{4-2}$$

where C_3 and ω_{mod} stand for the amplitude and frequency of the wavelength modulation. The functionality of the lock-in amplifier can be modeled by multiplying the output of the photodetector with the lock-in amplifier reference signal and integrating the product over several periods of the modulation signal, equivalent to taking the average of the product [41]. Therefore, the demodulated error signal is given by:

$$A_{err}(\lambda) = \int_{t=T}^{t=T+N/f_{mod}} \left(C_1 - C_0 \frac{2\alpha}{\alpha^2 + (\lambda + C_3 \sin(\omega_{mod} t) - \lambda_0)^2} \right) \sin(\omega_{mod} t + \phi) dt \tag{4-3}$$

This expression can be evaluated to reveal the characteristic shape of the error signal for peak locking around the absorption line center wavelength.

Figure 4-3 shows a simulated (normalized) error signal curve for wavelength modulation comparable to the α parameter and $\varphi = \pi$ for the necessary sign inversion. The Lorentzian lineshape of the absorption line is also plotted in the background as a reference.

49
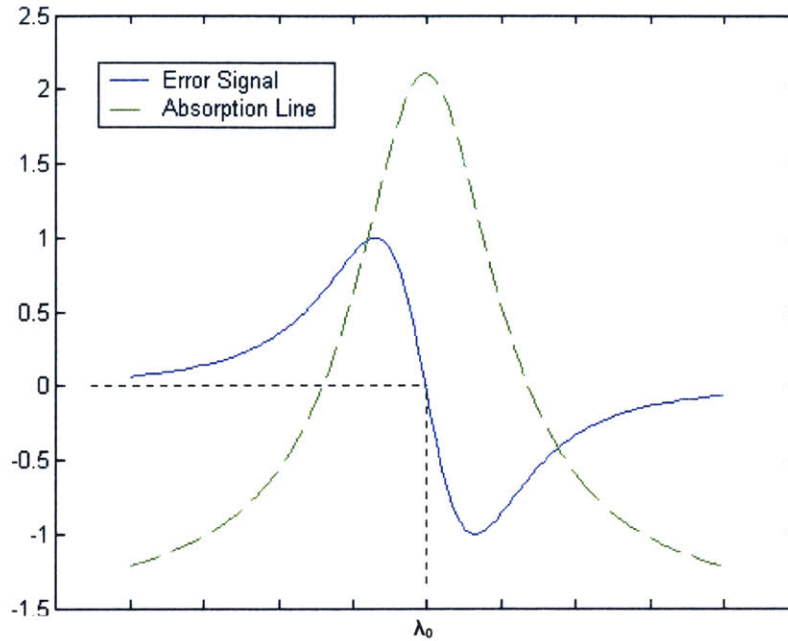
Figure 4-3   Characteristic error signal curve for peak locking wavelength stabilization

From Figure 4-3, it is clear that the error signal curve has the correct traits to counter drifts in the laser wavelength. At the absorption line center wavelength λ_0, the error signal is 0 and no adjustment to the laser current is made. If the diode laser wavelength wanders to higher wavelengths $\lambda > \lambda_0$, a negative error signal is fed back to the current source to decrease the bias current and ultimately the laser output wavelength. Similarly, if the laser wavelength drifts to lower wavelengths $\lambda < \lambda_0$, a positive error signal is supplied to the current source to increase the bias current and move the output wavelength back towards λ_0. Thus, the error signal properly corrects for differences between the laser wavelength and the absorption line center wavelength by changing the bias current of the diode laser and pushing the wavelength back to λ_0.

4.2 Experimental Realization of Peak Locking System

The process of putting together the peak locking system to lock the output wavelength of a diode laser was done in a very structured manner. Various characterizations were performed to gain a better understanding of system components, and also to provide adequate data to model the function of each component or group of components with reasonable accuracy. This data was later used to develop a Simulink model of the laser wavelength stabilization system. This section presents the characterization exercises in the order they were carried out for the logical construction of the eventual peak locking system. At the end of the section, the block diagram of the complete system is presented along with the results of a test to confirm that the system was successful in stabilizing the output wavelength of the diode laser.

4.2.1 Diode Laser Characterization

Knowledge of the dependence of the diode laser output characteristics on the control parameters was necessary to ensure operation of the laser well within the safety limits of those parameters while producing the desired output. In particular, the relationships between the output wavelength and the diode laser temperature and current were of great interest for the planned exercise. To investigate these relationships, the experimental setup shown in Figure 4-4 was used.
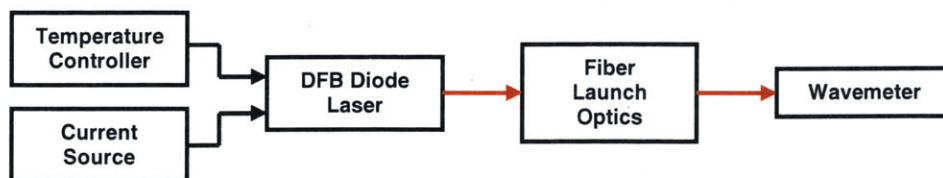
Figure 4-4 Block diagram of experimental setup for diode laser characterization

The DFB diode laser was housed in a Thorlabs (TCLDM9) mount that enabled temperature-controlled operation of the diode laser with an ILX Lightwave bipolar thermoelectric temperature controller (LDT-5910B) and low-noise current source (LDX-3620). Attached to the face of the mount was a fiber launch stage (Thorlabs KT112) consisting of a collimator, lens, and fiber adapter. The output light of the laser was coupled into optical fiber by the fiber launch optics, and sent to a wavemeter (Burleigh WA1500) to measure the wavelength.

Figure 4-5 Temperature dependence of diode laser output wavelength λ

First, the relationship between the diode laser output wavelength and the operating temperature was determined. The laser current was fixed by the current source at 200 mA while the temperature was varied from 22 °C to 27 °C, conservative operating limits for the diode laser, with a step size of 0.1 °C. At each temperature, the output wavelength was recorded from the

wavemeter. The data is presented in Figure 4-5. Several observations can be made from the experimental result. It is confirmed from Figure 4-5 that the nominal output wavelength of the diode laser is indeed 1532 nm. Also, the relationship between the laser output wavelength and operating temperature is revealed to be virtually linear. A simple linear fit of the experimental data indicates that the wavelength varies with temperature at a rate of 0.09737 nm/°C. This value agrees favorably with the 0.1 nm/°C wavelength temperature coefficient typically reported for diode lasers.

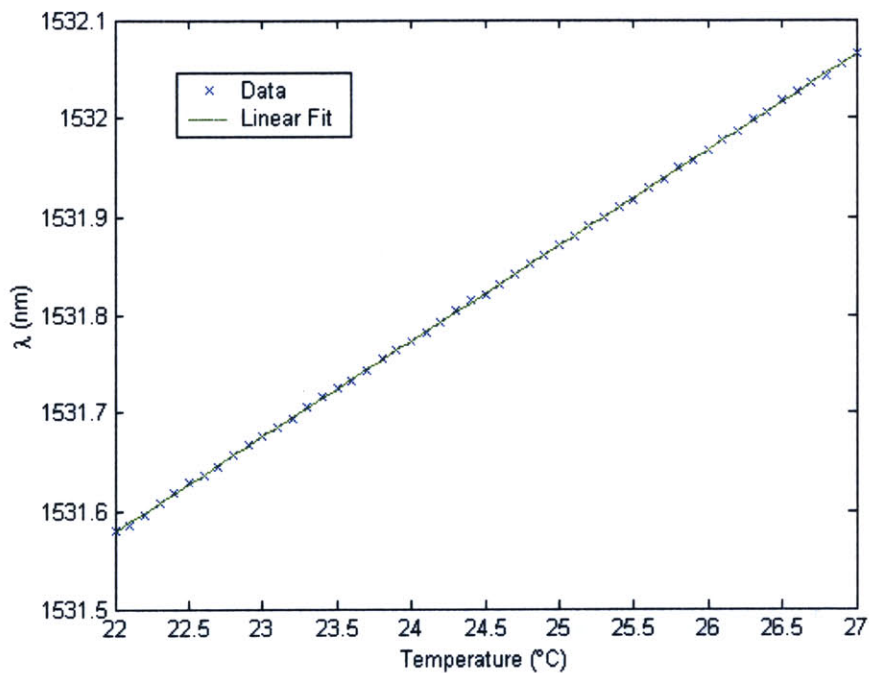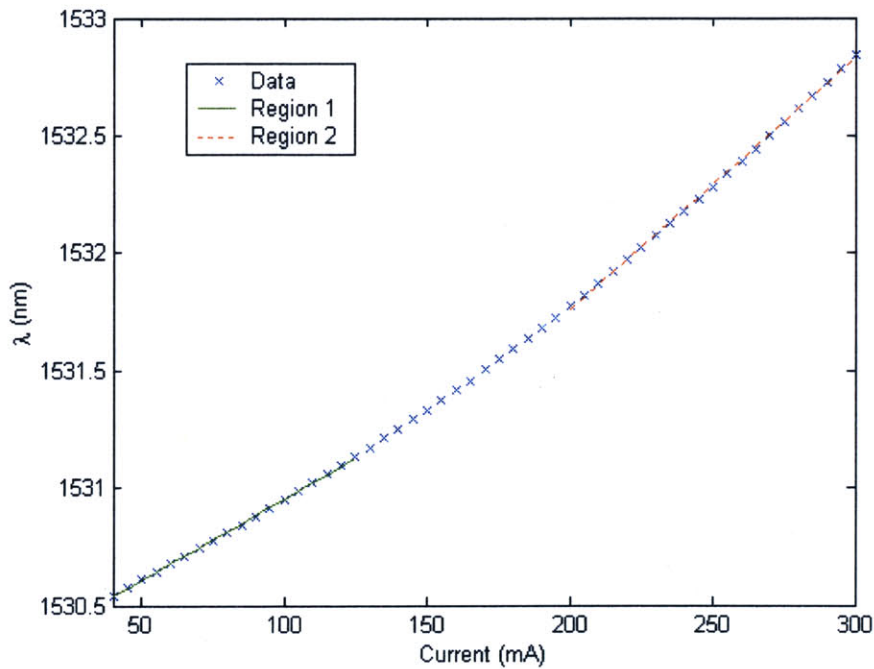**Figure 4-6 Current dependence of diode laser output wavelength λ**

The relationship between the diode laser output wavelength and current was determined similarly. The laser temperature was held constant at 24 °C while the drive current was scanned from 40 mA (threshold current ≈ 35 mA) to 300 mA with a step size of 5 mA. The output

wavelength at each current was measured by the wavemeter. Figure 4-6 shows a plot of the data that was obtained. Interestingly, the wavelength vs. current graph exhibits some curvature that indicates a higher sensitivity of wavelength to current at higher currents. Comparison of the sensitivities in region 1 and region 2 of Figure 4-6 reveals that the sensitivity is 0.00688 nm/mA for currents between 40 mA and 125 mA versus 0.01069 nm/mA for currents between 200 mA and 300 mA. To verify this trend, the data was retaken at a diode laser operating temperature of 22 °C. The sensitivities in region 1 and region 2 remained approximately the same at 0.00678 nm/mA and 0.00936 nm/mA respectively.

For completeness, the effects of the diode laser temperature and current on the output power were also characterized. Essentially the same experimental setup as the one depicted in Figure 4-4 was utilized, but the wavemeter was replaced by a photodetector (Thorlabs PDA255) and digital voltmeter. Since the sensitivity of the photodetector was very high ($\approx$ 9.5 V/mW), the light from the 20 mW laser had to be attenuated to avoid saturation of the photodetector ($\approx$ 10.4 V). Sufficient attenuation by a factor of 91.43 was achieved with the introduction of spacers at the photodetector input. To characterize the relationship between the diode laser output power and drive current, the current was varied from 0 mA to 125 mA with a step size of 5 mA, and the photodetector output voltage at each current was read from the voltmeter. Knowing the power-to-voltage conversion factor for the photodetector and the amount of attenuation at the photodetector input made it possible to calculate the unattenuated output power of the laser for each current data point. This experiment was performed three times at three different laser operating temperatures: 22 °C, 24 °C, and 27 °C. Qualitative comparison of the different sets of data at the very least provides some insight into how the diode laser temperature affects the output power. Figure 4-7 shows the obtained experimental data.
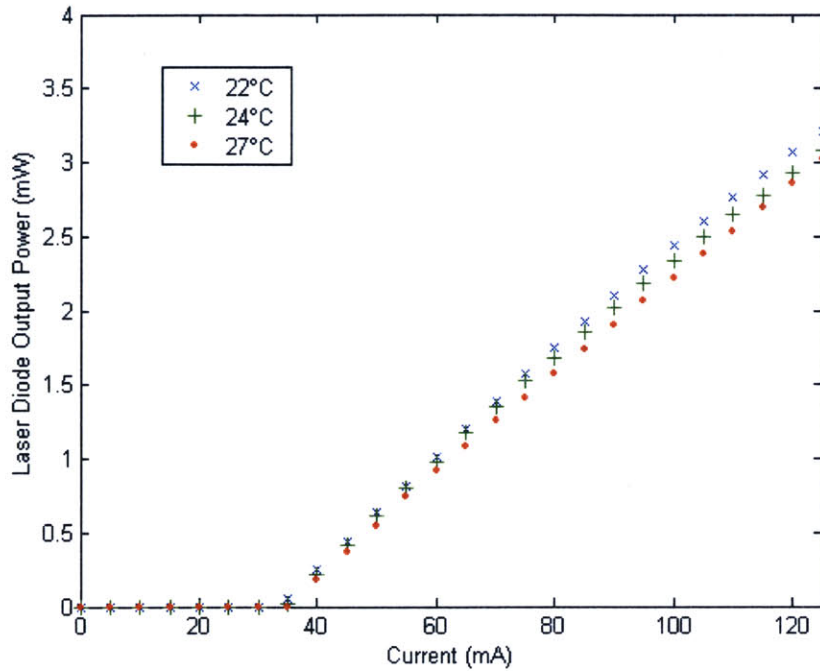
Figure 4-7   Characteristic diode laser output power/drive current curves

The curves n Figure 4-7 exhibit the behavior expected from a diode laser. It is apparent for all three curves that for laser currents less than some threshold current around 35 mA, there is no output light from the laser. For currents greater than the threshold current, the output power of the diode laser increases with the current. It is also evident that the (slope) efficiency of the laser decreases as the temperature increases. At 22 °C, the efficiency can be approximated from Figure 3-4 to be 0.0351 mW/mA. As the laser temperature increases to 24 °C and 27 °C, the efficiency falls to 0.0335 mW/mA and 0.0330 mW/mA respectively. Clearly, the output power of the diode laser is much more sensitive to changes in drive current than operating temperature, particularly in the conservative range of temperatures considered (22 °C to 27 °C).

Ultimately, power was not a serious issue in the process of locking the output wavelength of the diode laser to an absorption wavelength of acetylene. The 20 mW diode laser was

guaranteed to provide enough optical power at any reasonable operating point (temperature, current) to register a sizable voltage signal at the output of the photodetector. On the other hand, the output wavelength was not afforded the same degree of arbitrariness. To lock the wavelength of a laser to an absorption line, the wavelength must initially be near the absorption wavelength. The results of the diode laser characterizations presented in this section were used to select an operating temperature and current corresponding to the desired absorption wavelength. The next section covers the choice of absorption line.

4.2.2   NIR Absorption Lines of Acetylene (C$_2$H$_2$)

Acetylene gas is renowned for having strong absorption lines in the NIR spectral region. Figure
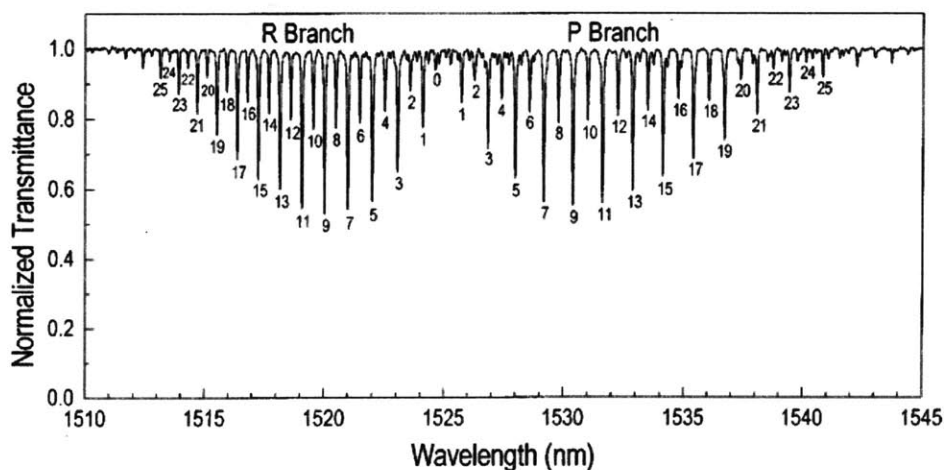
Figure 4-8   1510-1540 nm absorption spectrum of C$_2$H$_2$ [42]

4-8 depicts a portion of the NIR absorption spectrum of C$_2$H$_2$ from 1510 nm to 1540 nm. In the vicinity of the nominal output wavelength of the diode laser (1532 nm), there are several candidate absorption lines that the laser could be locked to: *P*10, *P*11, and *P*12. As it was

preferable to choose the most prominent absorption line available, $P10$ and $P12$ were ruled out, leaving $P11$ as the line of choice. According to the National Institute of Standards & Technology (NIST), the $P11$ absorption line of acetylene is located at a wavelength of 1531.5879 nm in vacuum. At higher pressures, there would be a shift of the line center wavelength, but it would be accompanied by broadening of the absorption line profile. In any case, operating the diode laser such that the output wavelength was close to 1531.5879 nm was expected to at the very least to correspond to a point on the $P11$ absorption lineshape.
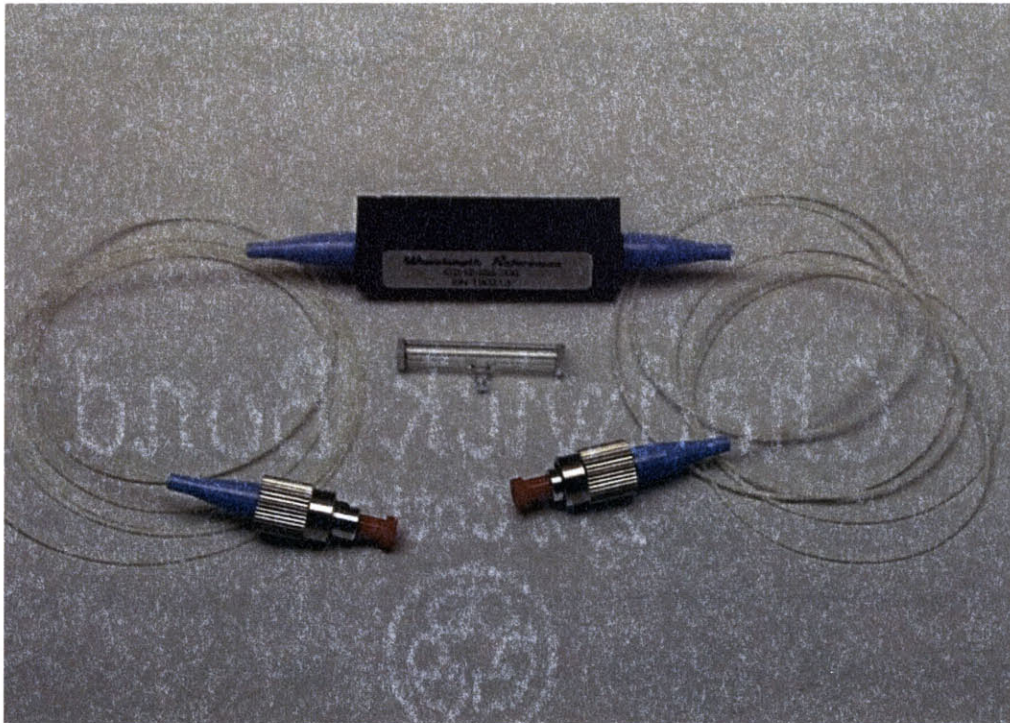
Figure 4-9 Wavelength References 200 Torr C$_2$H$_2$ gas cell [43]

A commercial fiber-coupled C_2H_2 gas cell from Wavelength References was used as the source of acetylene for the laser frequency stabilization exercise. An image of the gas cell is shown in Figure 4-9. The dimensions of the glass tube containing the acetylene (filled to 200

Torr) were 5 mm OD by 30 mm, and the dimensions of the aluminum housing where it was secured with silicone rubber were 4.7 cm by 1.4 cm by 1 cm. The C_2H_2 gas cell was outfitted with fiber pigtails, making it very convenient to couple light into the gas cell and pass the transmitted light to another fiber-compatible system component such as a photodetector. To find the $P11$ absorption line of the 200 Torr acetylene gas cell, the experimental setup illustrated in Figure 4-10 was utilized.
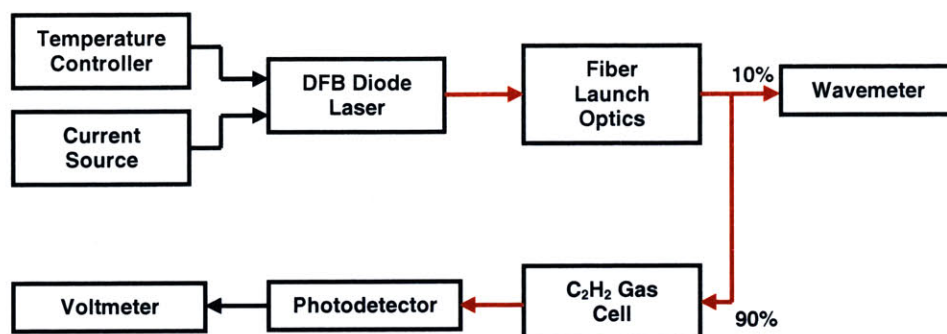
Figure 4-10   Block diagram of experimental setup for $P11$ line characterization

A 90/10 splitter was used to tap off 10% of the diode laser output power to be fed into the wavemeter where the wavelength was monitored. The rest of the output power was sent through the acetylene gas cell where absorption, if the wavelength was correct, occurred. The remaining transmitted optical power was converted to an electrical signal by the photodetector (with attenuation) and read by the voltmeter. Searching for the $P11$ absorption line of C_2H_2 was accomplished in two steps. First, the operating temperature and current of the diode laser were adjusted until the output wavelength, as measured by the wavemeter, approached the published vacuum wavelength of 1531.5879 nm. Next, the current was finely tuned about the established operating current until evidence of absorption i.e. attenuation was observed in the photodetector output. Current was chosen over temperature as the fine tuning parameter because the

58

wavelength tuning resolution of temperature was significantly poorer. The temperature controller was only capable of adjusting the operating temperature of the diode laser with a resolution of 0.1 °C. From Figure 4-5, this value corresponds to a wavelength tuning resolution of 10 pm. On the other hand, even a conservative estimate of the current source current tuning resolution of 0.1 mA leads to a wavelength tuning resolution of about 1 pm from Figure 4-6. The output wavelength of the diode laser was found to correspond to the $P11$ line of C_2H_2 at 200 Torr when the laser temperature and current were set at 22 °C and 200.1 mA respectively.

Figure 4-11 $P11$ absorption line of C_2H_2 at 200 Torr

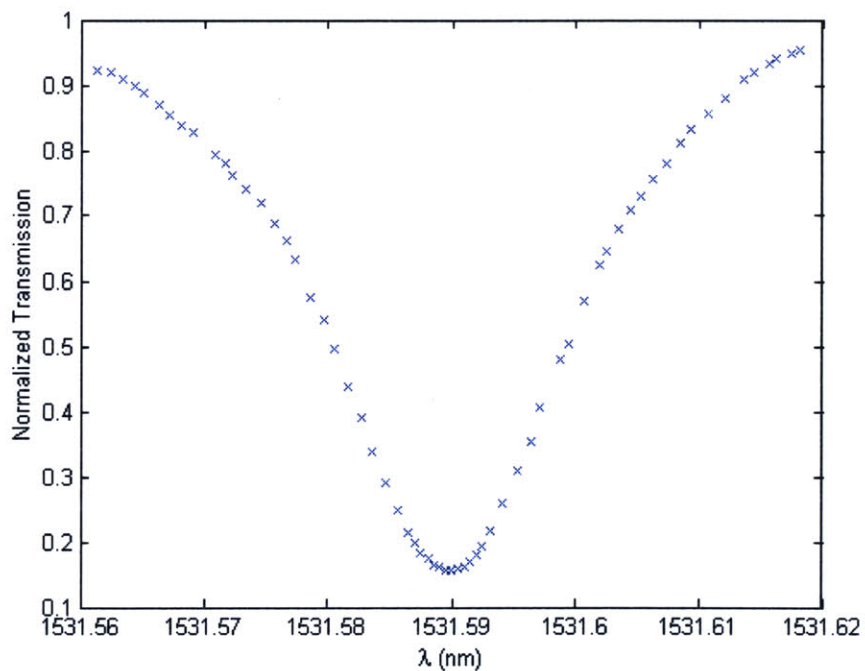The $P11$ line was characterized by finely scanning the diode laser current from 197 mA to 203 mA and simultaneously recording the output wavelength from the wavemeter and optical transmission from the voltmeter. The data acquired was used to generate the plot in Figure 4-11.

It is evident from Figure 4-11 that the $P11$ line is Lorentzian in shape as expected for a pressure-broadened absorption line. The FWHM linewidth is approximately 20 pm (2.5 GHz), which is typical in the pressure-broadened regime. The peak absorption wavelength of 1531.5897 matches favorably with the vacuum wavelength of 1531.5879 reported by the NIST for the $P11$ line of acetylene, and the positive wavelength (negative frequency) shift is consistent with the anticipation from theory. The peak attenuation at the absorption line center was 0.157 ($\approx$ -8 dB). Using the Beer-Lambert law, the absorption coefficient α associated with the $P11$ line can be estimated to be 0.6172 cm^{-1}. The difference in the depth of the $P11$ line in Figure 4-11 compared to the one shown in Figure 4-8 can be explained by the difference in acetylene pressures (200 Torr vs. 50 Torr) and gas cell dimensions (5 mm OD by 30 mm vs. unknown by 50 mm). Having selected, located, and characterized the $P11$ absorption line of C_2H_2, the next step towards the goal of locking the output wavelength of the diode laser to the $P11$ line was to verify that an error signal with characteristics as predicted in Figure 4-3 could be generated.

4.2.3 Error Signal Characterization

Theoretically, the error signal produced by a lock-in amplifier configured for peak locking should have a value of 0 at the absorption line center wavelength and opposite signs on opposite sides of it. To confirm that an error signal with these traits which are critical for stabilizing the diode laser output wavelength could be generated, the experimental setup shown in Figure 4-12 was used. The Sine Out output of a Stanford Research Systems SR850 100 kHz lock-in amplifier was utilized to generate the sinusoidal modulation signal necessary to dither the laser current via the external modulation input of the current source. This arrangement was convenient because the Sine Out signal was an internally generated signal of the lock-in

amplifier, and could double as an internal reference signal. The lock-in amplifier demodulated the error signal from the photodetector output. To characterize the error signal, the bias current supplied by the current source was varied from 197 mA to 203 mA, spanning the entire width of
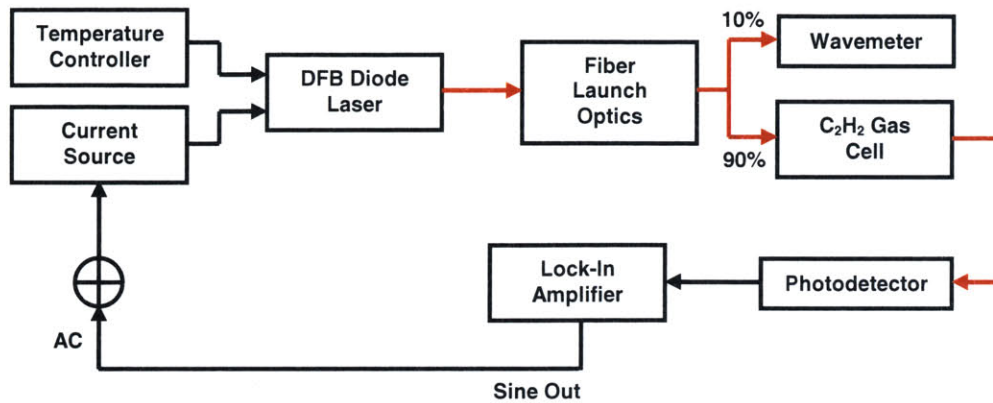
Figure 4-12 Block diagram of experimental setup for error signal characterization

the $P11$ line of C_2H_2 as illustrated in Figure 4-11 from 1531.56 nm to 1531.62 nm, while a constant small-amplitude dither around the bias current was created by feeding a 1 kHz 0.01 Vrms sinusoidal modulation signal generated by the lock-in amplifier through the summing junction and into the external modulation input of the current source. The summing junction was left in the system despite only having 1 input in order to preserve the relevance of the data obtained in the experiment to the final closed loop laser wavelength stabilization system. Data points were taken every few picometers, as monitored by the wavemeter, by recording both the laser output wavelength and the value of the lock-in amplifier X variable. At each data point, the sine modulation signal was first turned off to allow the wavemeter to measure the wavelength associated with the bias current, and then switched on to record the value of the X variable from the lock-in amplifier display.
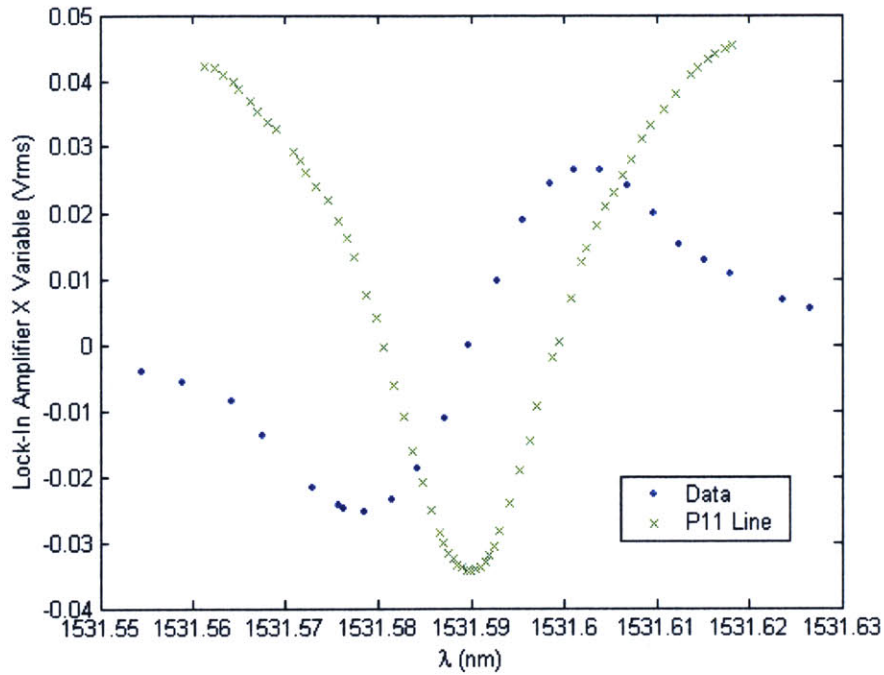
Figure 4-13 Demodulated error signal from lock-in amplifier w/P11 absorption line

Figure 4-13 plots the error signal as a function of wavelength, and also displays the P11

absorption line profile (units not relevant) as a reference curve. It is apparent from Figure 4-13

that the error signal demodulated by the lock-in amplifier does have the requisite characteristics

for locking the diode laser output wavelength to the absorption line center wavelength of the P11

line of acetylene at 1531.5897 nm. At this target locking point, the error signal has a value very

close to 0. Therefore, when the laser wavelength matches the wavelength at the absorption peak,

no adjustment to the wavelength is made. The error signal curve exhibits odd symmetry about

the zero-crossing at the locking point. While the signs of the error signal on either side of the

locking point are opposite from what is desired, negative for wavelengths less than 1531.5897

nm and positive for wavelengths greater than 1531.5897 nm, they can be inverted before they are

fed back to correct the diode laser bias current. What is more critical is that the error signal is

odd-symmetric about the locking point, which Figure 4-13 confirms. The eventual addition of sign inversion in the feedback path would enable the error signal shown in Figure 4-13 to be used for stabilizing the laser wavelength, increasing the bias current when the wavelength decreases from the absorption line center wavelength and decreasing the bias current when the wavelength increases.

The shape of the error signal curve as a function of wavelength meets the expectation from theory. When the output wavelength of the laser is scanned across the absorption lineshape with a small fixed modulation and $1f$ detection is performed with the lock-in amplifier, the anticipation is that the (phase-sensitive) demodulated signal as a function of wavelength will resemble the derivative of the absorption lineshape. The justification for this claim is that an infinitesimally small wavelength dither would yield a curve precisely proportional to the derivative of the absorption line profile. If the modulation of the wavelength is fairly small, then the demodulated signal as a function of wavelength can be expected to closely resemble the shape of the derivative. There are three points along the absorption line profile that clearly show the veracity of this assertion. At the absorption line center, the derivative is 0 as is the value of the error signal in Figure 4-13. Along the sides of the $P11$ line profile, near 1531.58 nm and 1531.60 nm, are located two points of maximum slope. The minimum of the error signal occurs very close to the location of maximum negative slope, and the maximum is located very close to the point of maximum slope.

The same principle applies when comparing the curve obtained from 2nd harmonic (or $2f$) detection with the lock-in amplifier and the error signal curve ($1f$ detection). Figure 4-14 depicts the $2f$ detection curve with the $1f$ detection curve from Figure 4-13 as a reference curve. It is

evident that the $2f$ curve has the shape of the 2nd derivative of the $P11$ line profile, or the

derivative of the $1f$ curve. At the absorption line center, the $1f$ curve has maximum slope. The $2f$
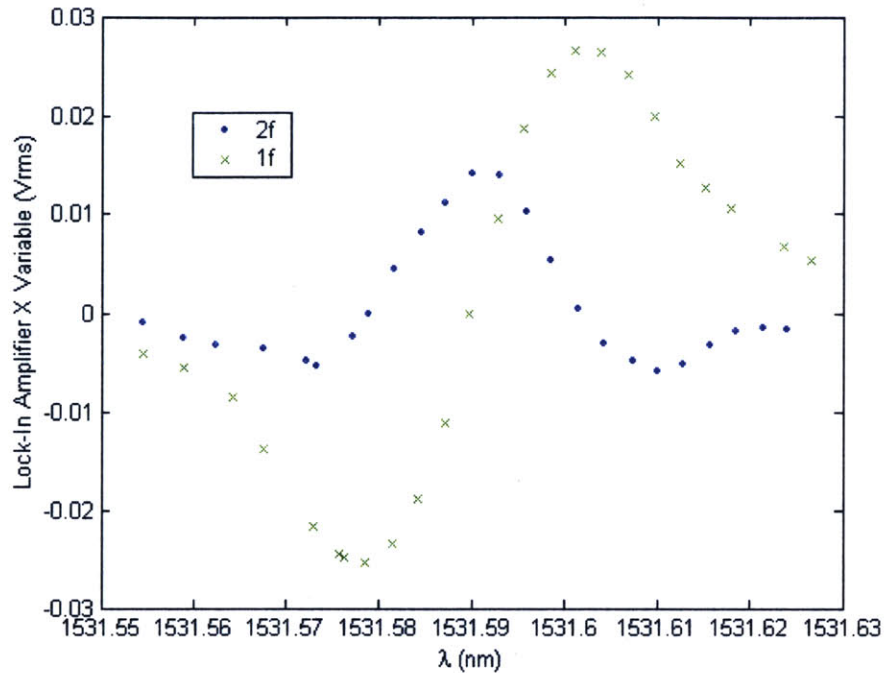
Figure 4-14 1f and 2f detection curves derived from $P11$ line of C_2H_2

curve exhibits a corresponding peak. At the minimum and maximum of the $1f$ curve, the slope is

0. The $2f$ curve has zero-crossings at those wavelengths.

4.2.4 Feedback Signal Transfer Function

The feedback (error) signal that is returned to the current source to adjust the bias current in

response to deviations of the diode laser output wavelength from the absorption line center is a

voltage signal. That signal bears some relationship to the resulting change in bias current that is

determined by the summing junction and the external modulation input of the current source. To experimentally determine the transfer function [mA/V] between the feedback voltage and the
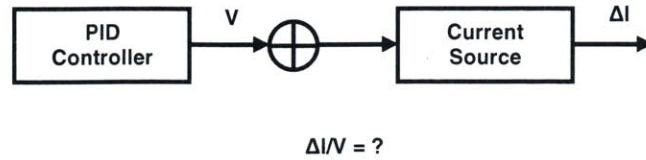
Figure 4-15   Block diagram of simple setup to determine feedback transfer function

resulting change in the laser bias current, the setup illustrated in Figure 4-15 was employed. The LR-130 PID controller was capable of outputting DC voltages of controllable amplitude. Therefore, it was used as a DC voltage source and the voltage was varied from 0 V to 0.05 V. The current was read from the display of the current source, with 196.5 mA being the no feedback bias current. The data collected from the experiment is shown in Figure 4-16.
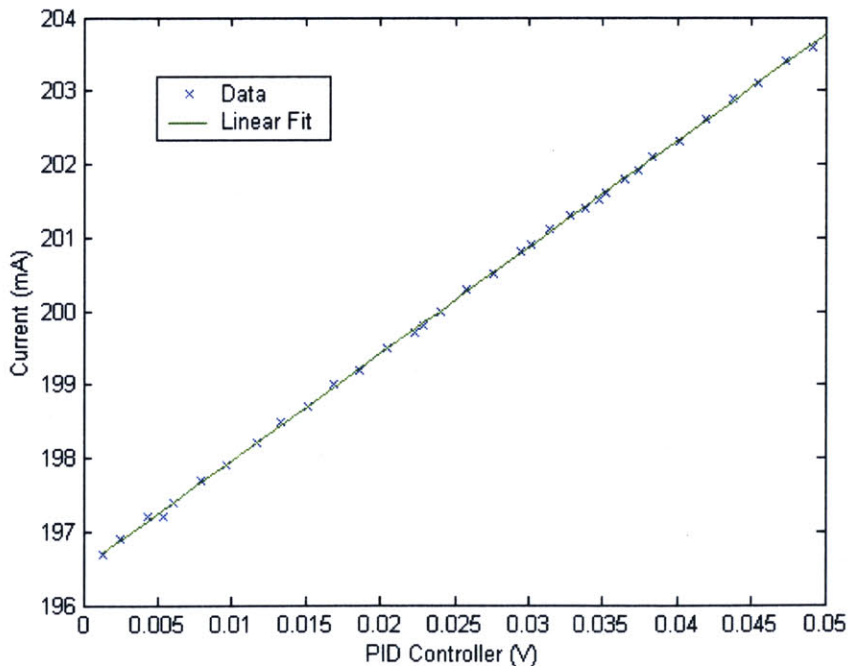
Figure 4-16   Bias current as function of feedback voltage to summing junction

From the data, the feedback voltage-to-current transfer function can be approximated to be 144.83 mA/V. This value is in the neighborhood of the theoretical value of 125 mA/V. The theoretical value was simply calculated from knowledge of the design of the summing junction and the manufacturer's specification for the transfer function of the current source external modulation input. As shown in Figure 4-17, the summing junction was just a resistor-divider network that inherently provided attenuation by a factor of roughly 0.5 to both the AC modulation signal and the DC feedback error signal. Given that the manufacturer's specification for the transfer function of the external modulation input of the current source was 250 mA/V, it was anticipated that the overall transfer function $\Delta I/V$ in Figure 4-17 would be 125 mA/V. The experimentally determined value of 144.83 mA/V represents an error of approximately 16% from the expected value. The error was attributed mainly to the current source external modulation input. The gain of the resistor divider was measured to be $\approx$0.52, a 4% error that indicated that the remaining 12% of error was due to the departure of the external modulation input transfer function from the 250mA/V manufacturer's specification.

LDX-3620 ext mod input

110k 110k

LR-130 output   SR850 sine out

(DC)
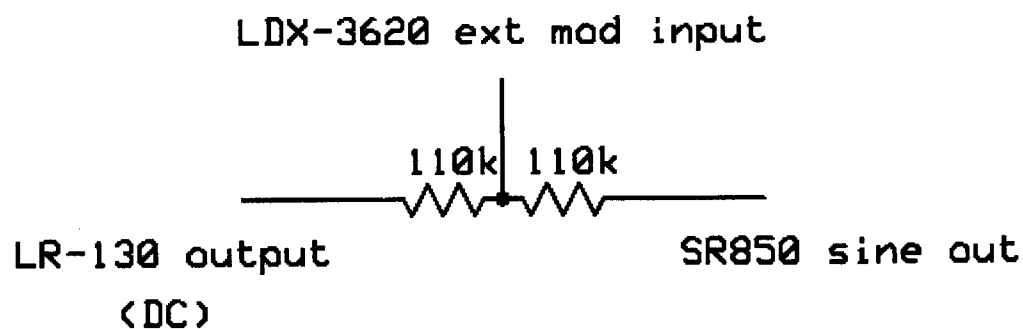
Figure 4-17 Resistor-divider network that served as summing junction

4.2.5 Laser Wavelength Stabilization System Parameter Values
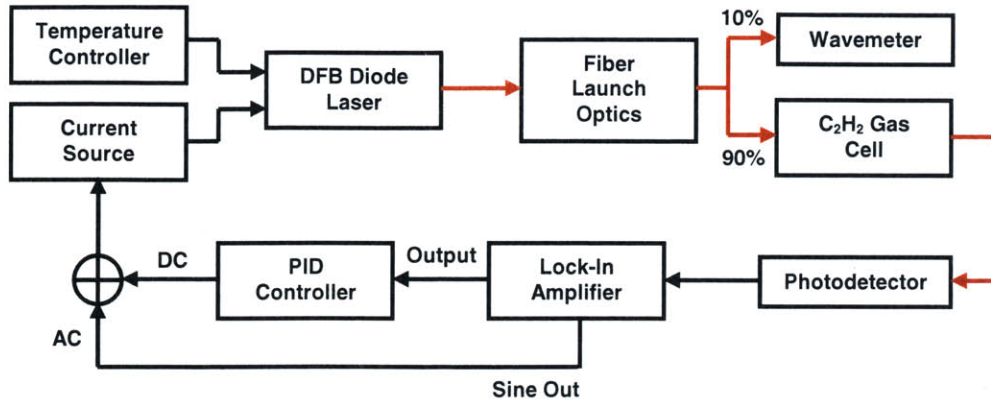
Figure 4-18 Block diagram of experimental setup for diode laser wavelength stabilization

The output of the lock-in amplifier was a DC voltage signal whose value was proportional to the value of the phase-sensitive X variable of the lock-in amplifier. Included in Figure 4-18 but excluded from Figure 4-2 is a PID controller (LR-130) which was required to supply the proper system dynamics in the feedback loop to achieve robust laser wavelength stabilization. In reality, the generic system depicted in Figure 4-2 would have failed to lock the laser wavelength to the absorption line if the value of the error signal was slightly imprecise. However, adding proportional and integral controls (at very least) to the feedback system, as illustrated in Figure 4-18, guaranteed that a reliable lock of the diode laser output wavelength would be accomplished with much less emphasis on the actual error signal amplitude. At the external modulation input of the current source, a summing junction was placed to add the constant AC modulation signal and a DC correctional feedback signal derived from the error signal demodulated by the lock-in amplifier.

The output wavelength of the DFB diode laser was successfully locked to the absorption

line center wavelength of 1531.5897 nm using the system illustrated in Figure 4-18. The

temperature of the diode laser was held constant at 22 °C, and the stabilized bias current at the

locking point was 200.1 mA. The modulation signal generated by the lock-in amplifier was a 1

kHz 0.01 Vrms sine wave. Demodulation was done by the lock-in amplifier with a low-pass

filter time constant of 30 ms and rolloff of 6 dB/oct (or 20 dB/dec), and the output was a voltage

signal proportional to the value of the X variable according to

$$V_{out} = (\frac{X}{sensitivity} - offset) \times expand \times 10V \qquad (4-4)$$

where the sensitivity was 1 V, the offset was 0 V, and the expand was 1. The proportional gain

of the PID controller was chosen to be 0.1, and the integral control whose circuit is displayed in

Figure 4-19 was also set to a value of 0.1, which specified the RC product.
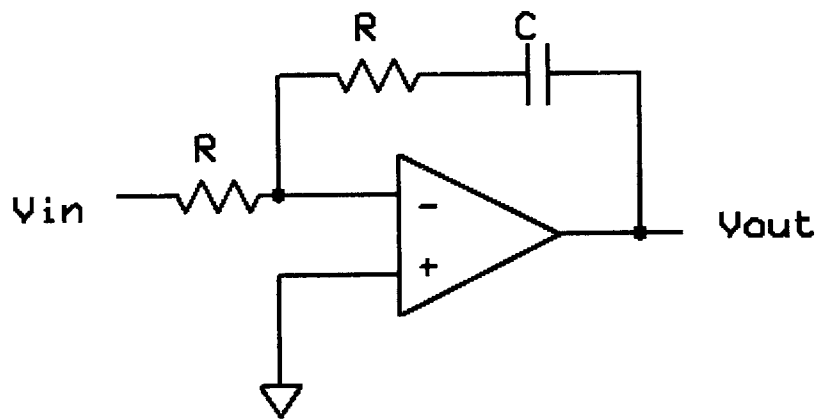
Figure 4-19 PID controller integral control circuit

The stabilization of the diode laser wavelength was confirmed by adjusting the bias

current with the current source while monitoring the photodetector output and the feedback

voltage from the PID controller in Figure 4-18. The photodetector output was observed to

68

remain unchanged for small perturbations of the bias current. For larger perturbations, restoration of the laser output wavelength was witnessed in real time as the photodetector output morphed back to the 2*f*-dominated signal characteristic of operation at the absorption line center wavelength (see Figure 4-14). When the bias current was increased using the control knob of the current source, a negative DC voltage was observed at the PID controller output, proving that the feedback signal was reducing the bias current back down to 200.1 mA. Conversely, when the bias current was decreased, a positive feedback voltage was evidenced at the PID controller output, again confirming that the system was restoring the bias current to 200.1 mA. The final confirmation of the system working is shown in Figure 4-20.
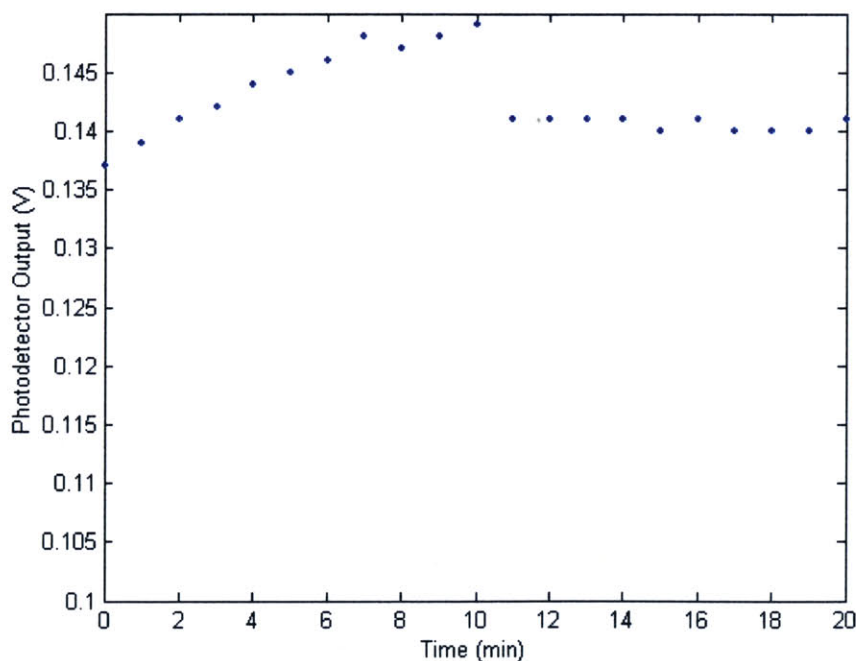
Figure 4-20   Proof of laser wavelength stabilization

The laser was operated open-loop, with the wavelength manually tuned to the absorption line center wavelength initially. Every minute, the output of the photodetector (see 4-18) was

recorded. After ten minutes, the feedback loop was closed to activate the laser wavelength stabilization system. Reading continued to be taken every minute for the next ten minutes. As seen in Figure 4-20, without the wavelength stabilizing feedback, the wavelength of the laser quickly drifted off the absorption line center wavelength for the $P11$ line of C_2H_2. Once the feedback loop was closed, the laser current was effectively stabilized and the output wavelength of the laser remained locked to the absorption line center wavelength. There is a small deviation of the locking point wavelength from the absorption line center. This shift is the result of the fact that in modulating the current of the laser, small amplitude modulation also occurs. This amplitude modulation manifests itself as a small shift of the error signal curve as demodulated by the lock-in amplifier. Therefore, the point of zero feedback is not precisely the absorption line center. However, for the particular diode laser used, the relative magnitude of the amplitude modulation was very small compared to the wavelength modulation, and the locking point remained close to the peak absorption wavelength.

Chapter 5

On Experimental Verification

A preliminary effort was made to demonstrate and characterize the performance of a photoacoustic gas sensing system utilizing hollow-core optical fiber as a novel resonant photoacoustic cell. This chapter consists of three sections. The first section presents the experimental setup put together to attempt to realize proof of concept of the theory developed in Chapter 3. The second section elaborates on the experimental procedures employed to try to produce meaningful results. Due to a number of unresolved issues encountered in the experimental process, results were unable to be obtained. These problems are detailed in the third and final section of this chapter, and must be addressed if future experiments are to yield fruitful results.

5.1 Experimental Setup

The experimental setup used featured electronics for the diode laser and acoustic signal detection and a simple vacuum system for handling the gas of choice. A 20 mW DFB diode laser with output wavelength near 1532 nm was utilized as the light source, and acetylene (C_2H_2) was chosen as the gas for experimentation on account of its strong absorption lines in the NIR spectrum, particularly in the vicinity of 1532 nm (see Figure 4-8). For clarity, the electronics and the vacuum system will be presented separately.

5.1.1 Electronics

Figure 5-1 shows a block diagram of the electronic equipment used and their connections.
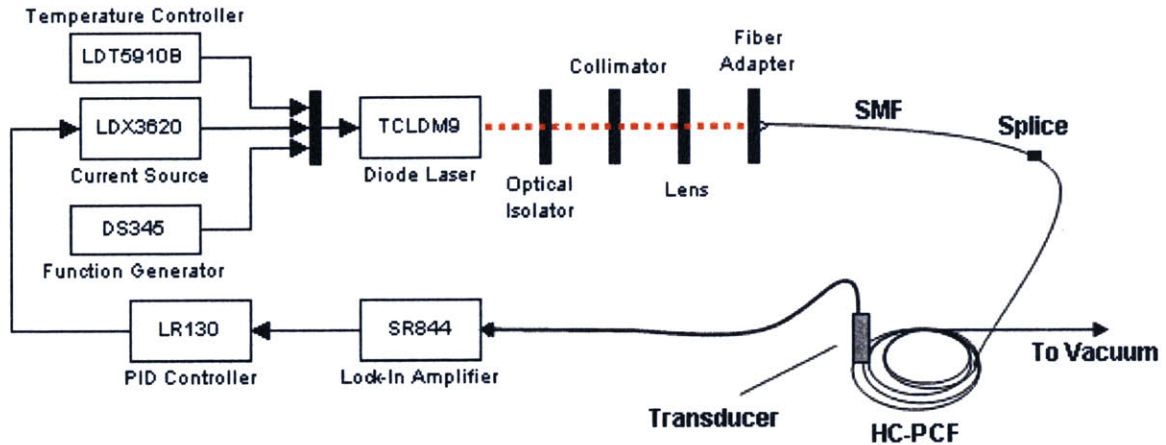
Figure 5-1 Electronics required for diode laser control and acoustic signal detection

The DFB diode laser was housed inside a Thorlabs mount (TCLDM9) which had three external input connections. An ILX Lightwave bipolar thermoelectric temperature controller (LDT-5910B) and low-noise current source (LDX-3620) were connected to the laser diode mount to control the output power and wavelength of the laser. In addition, a Stanford Research Systems 30MHz function generator (DS345) was the input source for the external RF modulation input of the laser diode mount, supplying the desired frequency (or wavelength) modulation of the laser output. The RF modulation input and the current source input were connected through an internal bias-tee network, allowing the DC bias current to be set by the current source while the AC modulation current was superimposed on top of it.

The laser diode mount interfaced directly with a fiber launch stage similar to the Thorlabs KT112 system to couple the output of the diode laser into single-mode optical fiber (SMF). The

fiber launch stage consisted of an optical isolator, collimator, lens, and fiber adapter in that order. XY and Z translators were available to adjust the positions of the lens that focused the collimated laser beam into the SMF and the fiber adapter that mates with the connector that terminated the SMF respectively. With these translational controls, the coupling efficiency of the fiber launch stage or the optical power in the fiber was able to be maximized.

The unconnectorized end of the SMF was fusion spliced to one end of a HC-PCF. This splice served two purposes: to create an airtight seal on one end of the HC-PCF so that the other end could be effectively placed in a vacuum system for fiber evacuation and gas filling, and to preserve the capability to inject light into the core of the HC-PCF. The HC-PCF was wound loosely into a coil of diameter $\approx$3", and the resulting turns of fiber were used to cover the majority of the 0.25" diameter sensing element of an NDT Systems ultrasonic transducer that was placed on top of the HC-PCF to detect the PA signal at the outer surface of the fiber. This measure was necessary to ensure that the total acoustic energy incident on the sensing element of the transducer was sufficient to displace it and produce an electrical signal large enough to be detected by the chosen electronics. To reduce the extremely large acoustic impedance mismatches at the fiber-air and air-transducer interfaces which would have resulted in very poor coupling of the ultrasonic PA signal from the HC-PCF to the transducer, glycerin was applied between the fiber and the transducer as an ultrasonic couplant.

Since the signal of interest was at a specific known frequency, simulated to be around 8 MHz in Chapter 3, an RF lock-in amplifier was used to measure its amplitude. The modulation source doubled as the external reference for the lock-in amplifier. The lock-in amplifier was synchronously utilized to produce the error signal required for stabilizing the wavelength of the diode laser (as discussed in Chapter 4). Although the reference for peak locking in this setup is

the PA representation of the absorption line and not the transmission through the absorption line, the principle is the same, as is the shape of the error signal curve.

5.1.2 Vacuum Setup

A vacuum system based on QF components was built to allow the HC-PCF to be filled with gas of choice, C_2H_2. Figure 5-2 depicts a schematic of the system. The vacuum system featured a central cross structure with four ports. The HC-PCF was interfaced to one of the ports. The
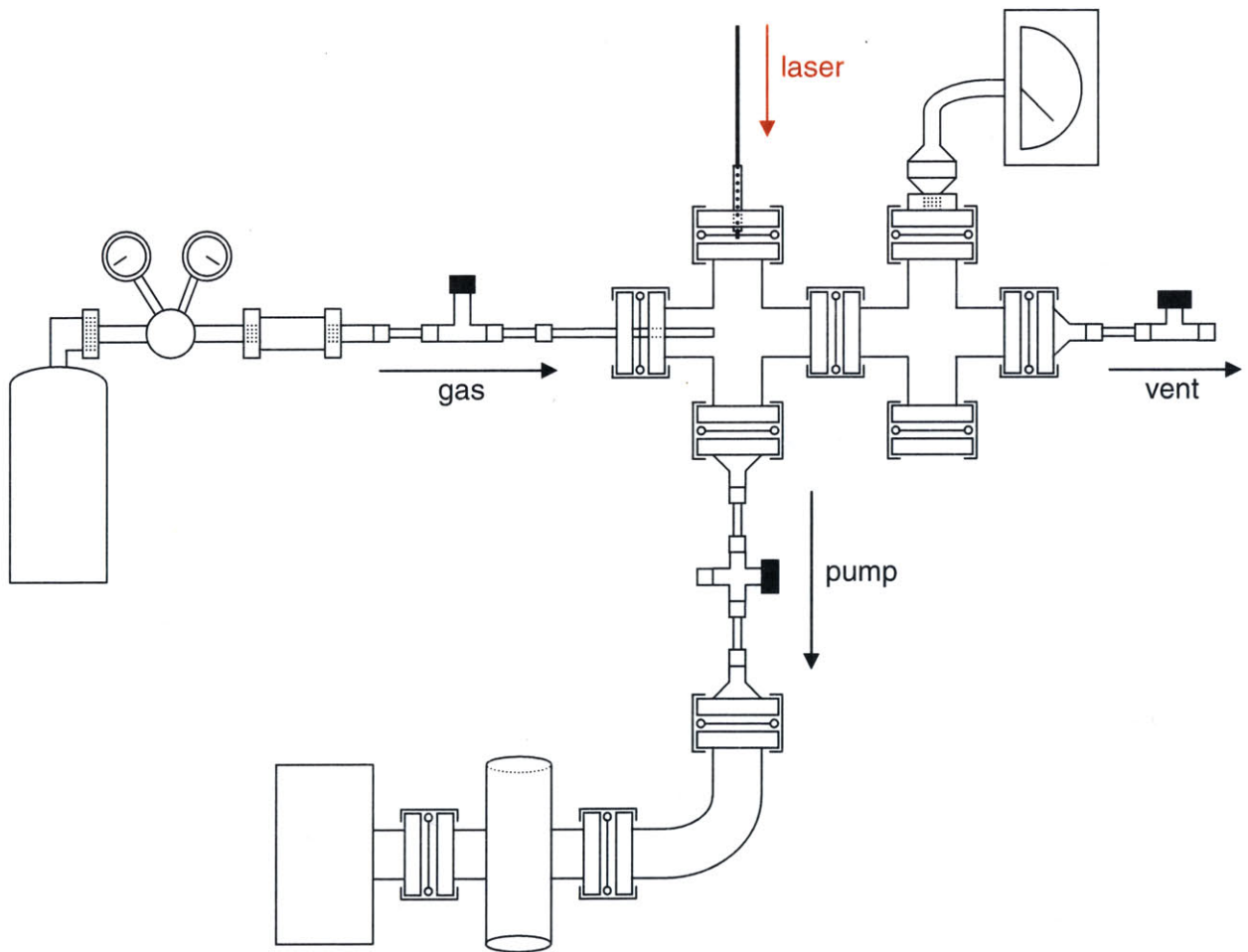

Figure 5-2 Vacuum system for HC-PCF gas filling and evacuation

fiber was epoxied into an optical fiber ferrule, which was then epoxied to a blank flange that was clamped into the port. Connected to another of the ports was a rough mechanical pump with a foreline trap, flexible PVC tube, and 3-way valve. This pump was used to evacuate the vacuum system, and ultimately the core of the HC-PCF. The foreline trap was necessary as a precautionary measure to prevent oil from the pump from traveling into the vacuum system. A 3-way valve was employed also to eliminate the possibility of oil migrating into the vacuum setup. Unlike a 2-way valve, a 3-way valve allows the vacuum pump inlet to vent to atmospheric pressure in the off state. Therefore, the pressure gradient is never suitable for pump oil migration into the vacuum setup. The last two ports of the main vacuum structure were dedicated to the gas supply and pressure gauge. An atomic absorption grade C_2H_2 cylinder was obtained and connected to the vacuum setup through a proper regulator, flash arrestor, and needle valve. The regulator set the outlet delivery pressure and the needle valve controlled the flow rate of C_2H_2. The flash arrestor was a safety device capable of shutting off the flow of C_2H_2 and putting out the flames before they reached the cylinder if C_2H_2 were to ignite. The final port of the system was connected to another set of auxiliary ports, to which a vacuum pressure gauge and vent valve were interfaced.

Operation procedures for the vacuum system were as follows. For evacuation of the HC-PCF, the needle valve controlling the flow of C_2H_2 into the system was closed as was the vent valve. The 3-way valve located in the path of the pump was switched to its "on" position, opening up the path for air/gas to be pulled out of the system. The pressure inside the vacuum system was monitored by the pressure gauge, which was able to measure pressures down to 1 mTorr. Given enough time, the pressure inside the core of the HC-PCF would equate itself to the pressure inside the chamber in which the open end of the fiber resided.

Once the core of the HC-PCF was successfully evacuated, it could be backfilled with gas to the desired pressure. The pump valve was shut off, the delivery pressure was set using the regulator, and the needle valve was opened to allow C_2H_2 to flow into the vacuum setup. Given time, the pressure inside the chamber would reach the desired pressure set by the regulator, and that pressure of C_2H_2 would also have filled the core of the HC-PCF.

5.2 Proposed Experimental Procedures

With the experimental setup detailed in section 5.1, a series of experiments were attempted. The aim of these experiments was to extract meaningful data on the performance of the system, not only in terms of detection sensitivity of PAS done with a HC-PCF PA cell, but also in terms of practical considerations such as the evacuation and filling times of the HC-PCF. This section outlines several experiments that were intended to yield the desired data.

5.2.1 Determination of HC-PCF Resonance Frequency

The first order of business was to confirm the ANSYS simulation results for the resonance frequency of the first radial mode of the HC-PCF structure. The wavelength modulation frequency was tuned in the neighborhood of 8 MHz while the lock-in amplifier measured the PA signal. A plot of the amplitude of the PA signal as a function of modulation frequency was expected to yield a resonance peak attributed to the mechanical resonance of the HC-PCF with a resonance quality factor that could be compared to the estimation from theory. Since there was much doubt as to the validity of applying equations for solid cylinders for first-order analysis of the resonance quality factors of HC-PCFs, this experiment would have shed some light on the matter.

5.2.2 HC-PCF Gas Evacuation and Filling Times

Assuming that a PA signal could be detected by the ultrasonic transducer, the dynamics of loading a gas into or removing a gas from the HC-PCF could be determined. First, the HC-PCF would be evacuated for a long period to ensure that all gas has been removed from the core. Then, it would be loaded with C_2H_2 to a pressure where the location of the target absorption line was known i.e. 200 Torr from Chapter 4. With the diode laser wavelength tuned to the absorption line and wavelength modulation applied, the measured signal from the lock-in amplifier ($2f$ detection) in Figure 5-1 would be recorded as a function of time. The anticipated form of the data would be a rising exponential, where the amplitude of the PA signal eventually settles at its final value as the gas finishes loading into the core of the HC-PCF. Similarly, the evacuation time of the HC-PCF could be determined by monitoring the signal amplitude measured by the lock-in amplifier as a function of time. The expected form of the data in this case would be a decaying exponential, where the amplitude of the measured signal dies out as the gas is removed from the core of the fiber. To verify the repeatability of the results, and also to address the concern of C_2H_2 molecules sticking to the walls of the HC-PCF, these evacuation and gas-filling experiments would be run several times in succession.

5.2.3 Detection Sensitivity

The detection sensitivity was intended to be analyzed by taking measurements of the PA signal at various pressures of the gas being sensed, C_2H_2. The locations of the absorption lines for each pressure would have to be determined in advance by scanning the laser wavelength (with modulation) until a PA signal was detected. Once located, the absorption lines could be locked

to by the laser wavelength and accurate measurements of the PA signal could be taken. Theoretically, the amplitude of the PA signal should vary linearly with the pressure of the detected gas. The data from the proposed experiment would have been able to confirm this trend. Characterization of the noise is also necessary for analysis of the sensitivity. This data was planned to be obtained through PA experiments with either an evacuated HC-PCF core or an air-filled HC-PCF core. In either case, no absorption of the light would be expected and consequently no PA signal would be expected to be observed. Combining the accumulated data from the PA signal and noise experiments, signal-to-noise ratios could be calculated to quantify the detection sensitivity of the system.

5.2.4 Preliminary Analysis of Acoustic Coupling

The HC-PCF was coiled to provide more acoustic energy to displace the sensing element of the ultrasonic transducer. It was of interest to firmly establish that this coiling actually made a difference. First, measurement of the PA signal would be attempted without coiling the fiber. In this case, minimal signal would be anticipated due to the tiny contact area between the flat sensing surface of the transducer and the round HC-PCF. PA measurements would then be made with coils of successively greater numbers of turns. The amplitude of the PA signal would be expected to increase as the coupling area between the HC-PCF and the transducer increases. This observation would have shown that coiling the HC-PCF was indeed beneficial for the measurement of the PA signal. Time permitting, other designs to couple the PA signal into the ultrasonic transducer would have been explored.

5.3 Preliminary Results

Attempts to execute the experiments discussed in section 5.2 were largely unsuccessful. The PA signal was unable to be observed, making it impossible to gather the data that was desired. In troubleshooting, it was found that the problem definitely did not lie with the loading of C_2H_2 into the core of the HC-PCF. To prove this to be true, a gas-loading experiment was run. The vacuum system was utilized to pump all gas out of the core of the HC-PCF down to roughly 10 mTorr. This process took several hours. Next, a relatively high pressure of C_2H_2 of 200 Torr was bled into the vacuum chamber. Theoretically, the pressure gradient between the core of the fiber and the vacuum setup would force the C_2H_2 into the HC-PCF. The gas was left to fill the core of the HC-PCF over the course of 30 min. After 30 min, the HC-PCF was removed from the vacuum system and quickly clamped into place in front of a power meter. The transmission
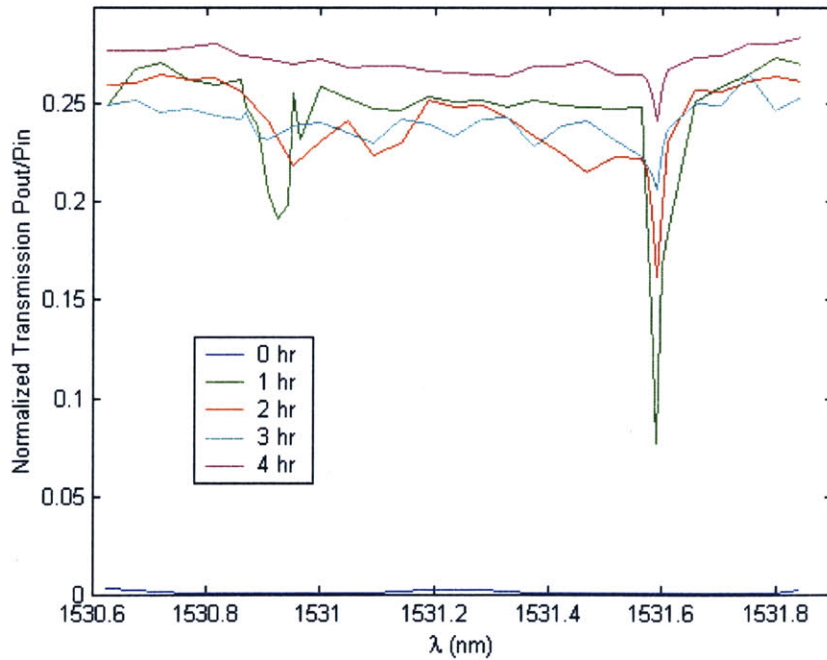

Figure 5-3   Proof of C_2H_2 inside core of HC-PCF

spectrum through the HC-PCF was recorded by tuning the bias current of the diode laser and measuring the transmitted power with the power meter. The HC-PCF was then immediately replaced in the vacuum system and pumped for 1 hr. Measurement of the transmission spectrum was repeated. This cycle of evacuation and measurement was continued for several hours. The results of this test are shown in Figure 5-3.

The normalized transmission through the HC-PCF is plotted against the diode laser output wavelength. The curve labeled "0 hr" corresponds to the data taken immediately after the gas-filling process was completed. The shape of the curve can be explained by the fact that the absorption was too great at this point for the power meter to measure any transmitted light i.e. it bottomed out, and the ongoing diffusion of air and C_2H_2 in and out of the HC-PCF created the severely broadened lineshapes. As the core of the HC-PCF was progressively evacuated, it is apparent that the absorption lineshapes started to grow weaker. By the time the 4th evacuation had been completed, one of the absorption features was no longer visible. Therefore, there is solid evidence that the gas-filling process for the HC-PCF does work, and the difficulties experienced in trying to detect the PA signal were not caused by an ineffective gas-loading method. Comparing the observed absorption spectrum in Figure 5-3 with the absorption wavelengths published by the NIST for C_2H_2, it is apparent that the observed absorption was due to the $P10$ and $P11$ absorption lines of C_2H_2 at approximately 1531.9763 nm and 1531.5879 nm respectively.

Although the theory governing the evacuation and filling times of HC-PCFs is still being investigated, it is informative to examine the literature and see what has been reported. A 0.8m long HC-PCF was successfully evacuated of C_2H_2 at pressures of 10 mbar ($\approx$ 7.5 Torr) and 113 mbar ($\approx$ 85 Torr) in 30 min and 1 hr respectively in one study [8]. The associated filling times

were 6 s and 4 s respectively. In another study, a 1.39 m and a 6.35 m long HC-PCF were reported to have similar evacuation and filling times of approximately 3 min and 30 min respectively regardless of pressures between 8.5 Pa ($\approx$ 0.064 Torr) and 149 Pa ($\approx$ 1 Torr) [44]. Obviously, the evacuation and filling dynamics depend greatly on the length of the HC-PCF used, the pressures the fiber is filled to with the gas, and the type of vacuum pump in the system. Qualitatively, higher pressures can be expected to lead to shorter filling times but longer evacuation times, and these times can be expected to increase with fiber length nonlinearly such that they increase faster than the fiber length [44]. Therefore, an evacuation time on the order of several hours for a length of HC-PCF between 2 and 3 m, which Figure 5-3 suggests is the case, seems reasonable.

5.4 Unresolved Experimental Issues

The inability to detect a PA signal could have been caused by a number of culprits. First, the ultrasonic transducer might not have been sensitive enough. The transducers that were obtained were designed for flaw detection and consequently were heavily damped. These transducers were essentially tiny piezo pieces that were designed to sense or resonate at a particular frequency e.g. 5 MHz or 10 MHz. The damping provided enabled a typical bandwidth, as measured between -6 dB points, of roughly 100%, meaning that a 5 MHz transducer would be able to sense frequencies from 2.5 MHz to 7.5 MHz for example. Due to the bandwidth-sensitivity tradeoff of the transducers, the sensitivity might have been rather limited. However, solving this problem is not entirely trivial in that some bandwidth i.e. damping of the transducer sensing element is necessary to be able to experimentally verify the mechanical resonance frequency of the HC-PCF as described in section 5.2.1. Piezo sheets of high sensitivity are

commercially available, but these undamped transducers would only be able to detect signals at frequencies in the immediate vicinity of their resonance frequencies. Furthermore, to couple the PA signal into one of these transducers, a hard couplant e.g. superglue is recommended. Considering the cost of HC-PCF, implementing such a permanent setup would be undesirable, especially in the event that the setup was ineffective and had to be removed.

Another potential problem that may have prevented the PA signal from being detected is the coating on the HC-PCF. In all of the analysis thus far, there has been no mention of the fiber coating and what its effects on the acoustic signal might be. It was not assumed that the fiber coating material was insignificant in the analysis. Instead, the material properties of these coatings are generally not well known or investigated, and consequently conjecturing on their possible effects on the amplitude of the PA signal was difficult. There is evidence, however, that fiber coatings can have adverse effects on coupling the PA signal out of the HC-PCF [45]. In particular, UV curable acrylates have been found to be least optimal for coupling acoustic signals into or out of optical fibers. Since the HC-PCF had a single-layer acrylate coating, the PA signal might have been severely attenuated in the acrylate coating before it reached the ultrasonic transducer.

The obvious solution to this problem would be to remove the coating of the HC-PCF and expose the transducer directly to the surface of the fused silica structure. Unfortunately, the removal of the fiber coating without damaging the surface of the optical fiber inside is difficult to accomplish. Mechanical methods of stripping the fiber coating e.g. using a razorblade are most risky, but even less abrasive methods such as using chemical solvents can compromise the structural integrity of the optical fiber. For instance, the practice of immersing optical fibers in acetone to remove coatings was found to reduce the mechanical strength of the fibers [46]. The

effect was especially apparent for optical fibers with single-layer acrylate coatings, which is what the HC-PCF had. As the idea of using HC-PCF as a PA cell relies on its mechanical resonance properties, stripping the coating off of the fiber was a risky proposition at best.

Finally, the lack of a way to monitor the optical transmission through the HC-PCF caused major problems. Without the capability to observe the transmitted light intensity through the HC-PCF, it was impossible to know for sure whether or not the diode laser wavelength was on the target absorption line feature. The only possibility for experimentation was to fill the HC-PCF with C_2H_2 at 200 Torr, where the location of an absorption line was known from the characterization performed in Chapter 4. However, at this relatively high pressure, the absorption coefficient for C_2H_2 is large (estimated to be 0.6172 cm^{-1} in section 4.2.2) and the optical power in the fiber decays quickly. Therefore, the generated PA signal would be strongest at the beginning of the HC-PCF and almost nonexistent by the end. In this case, coiling the fiber would not help to increase the acoustic energy coupled to the transducer. Moreover, the distribution of the acoustic signal in the coil of HC-PCF would result in poor coupling due to the size mismatch between the transducer sensing element and the single turn of fiber containing the majority of the PA signal.

Chapter 6

Conclusion

6.1 Summary

A brief overview of basic absorption-based laser spectroscopic techniques such as conventional laser absorption spectroscopy (LAS) and wavelength modulation spectroscopy (WMS) provided a pathway to discuss the established merits of photoacoustic spectroscopy (PAS) and hollow-core photonic crystal fiber (HC-PCF) for high-sensitivity gas sensing in Chapter 2. In Chapter 3, the proposed integration of HC-PCF into PAS as a novel mechanically resonating gas cell was introduced. Through analysis of classical PA theory, it was determined that the key parameters to evaluate to assess the overall feasibility and performance of this conception were the cross-sectional area, resonance frequency, and resonance quality factor of the HC-PCF. These parameters were analyzed using a combination of simulation results and empirically determined equations reported in a number of publications. The chapter concluded with a first-order estimation of the amplitude of the PA signal that could be expected in the absence of coupling inefficiencies into a suitable transducer. Chapter 4 addressed the implementation of laser wavelength stabilization, necessary for the accurate measurement of data. Both theory and experimental realization of were discussed. Finally, Chapter 5 elaborated on the experimental verification of the theory in Chapter 3. The experimental setup that was constructed and the procedures that were attempted were detailed. Concluding the chapter was a discussion of the

main problems confronted during experimentation, namely the reasons why a PA signal was unable to be observed.

6.2 Recommendations for Future Work

Many areas of the thesis work could use further study or refinement. These areas include the theoretical development of the project idea and the experimental setup assembled to verify the theory.

6.2.1 Theoretical Development

In much of the analysis presented in Chapter 3, the governing equations of classical PA theory were assumed to apply (to first order) to the case of PAS using HC-PCF as the PA cell. However, this assumption may be invalid since the gas cell is traditionally regarded as a rigid body in PA theory, whereas the HC-PCF is proposed to be a mechanically resonating structure. Therefore, it would be of great interest to develop the theory to derive the expression for the amplitude of the PA signal and its dependencies on system parameters. This calculation would be a revision to the acoustic signal generation theory presented in section 3.1.2. The inhomogeneous wave equation would still apply, but the boundary conditions for the acoustic signal at the walls of the gas cell would be different. Ultimately the goal would be to derive a more accurate expression from which the PA signal amplitude could be estimated. Another approach would be to use simulations to study the dependencies of the amplitude of the PA signal produced by the resonating HC-PCF on the HC-PCF dimensions, resonance frequency, quality factor, etc. If it could be shown that the dependencies remain the same as for conventional PAS, then the theoretical analysis presented in this thesis would gain support.

6.2.2 Modifications to Experimental Setup and Procedures

Given the difficulties experienced with the experimental setup described in this thesis, the emphasis of the recommendations for future work is on the experimentation. The most immediate modification that should be made to the experimental setup if the research is to be continued is the addition of a way to constantly monitor the light transmission through the HC-PCF. Typically, in vacuum setups involving HC-PCFs, the optical transmission is made accessible by butt-coupling the light from the HC-PCF into a multimode fiber (MMF) with a V-groove for alignment [8]. The gap between the two fibers is usually on the order of tens of microns, small enough such that sufficient light is coupled into the MMF and large enough such that the transport of gas into or out of the HC-PCF is still possible. The other end of the MMF is exited from the vacuum setup in the same way that the HC-PCF was interfaced to it, and run to a photodetector to measure the optical power. If this method of monitoring the optical transmission through the HC-PCF could be implemented in the existing vacuum system, then experimentation would be greatly advanced. Most importantly, it would be possible to know that the laser wavelength was on an absorption line, for any pressure of C_2H_2. Moreover, data concerning the gas-filling and evacuation times of the HC-PCF would be easily obtained. While maintaining the laser wavelength at an absorption wavelength, the photodetector output could simply be read over time during the course of a filling or evacuation process.

The world of MEMS promises transducers of superior sensitivity and miniature size. The growing field of capacitive micromachined ultrasonic transducers (CMUTs) could offer a transducer of sufficient sensitivity and bandwidth since the performance characteristics are highly tailorable by design [47]. Another avenue of pursuit in the realm of MEMS is the development of pressure sensors that fabricated on an end of an optical fiber [48, 49]. Figure 6-1

shows the configuration of the pressure sensor. The pressure sensor is based on the Fabry-Perot interferometer where a silicon

Figure 6-1 Pressure sensor fabricated onto end of optical fiber [48]

diaphragm anodically bonded to the end of the optical fiber and the fiber-etched cavity interface serve as the reflectors of the interferometer. The light reflected from the pressure sensor is spectrally shifted and detection of that shift leads to a measure of the pressure displacing the diaphragm [48]. While this technology has yet to be extended to ultrasonic frequencies, it has promise because the sensor has dimensions equal to the diameter of the optical fiber. If the pressure sensor were to be fabricated on the end of an optical fiber of equal size to the HC-PCF, then the acoustic coupling between the sensor and the PA signal emanating from the HC-PCF would be vastly improved over much larger transducers. In sum, the world of MEMS provides options for miniature high-sensitivity ultrasonic transducers that may be capable of compensating for the presence of an attenuating fiber coating layer.

If the transducer sensitivity cannot be improved, then the last resort would be to explore ways of increasing the optical power sourced to the core of the HC-PCF. One could reference various publications reporting optimal splicing parameters to minimize the splicing losses of SMF to HC-PCF [50, 51]. More significantly, the laser power could be increased by several orders of magnitude by employing an erbium-doped fiber amplifier. These measures should theoretically boost the amplitude of the generated PA signal since the PA signal is expected to be directly proportional to the sourced optical power.

References

[1]   A. T. Case, D. Tan, R. E. Stickel, and J. Mastromarino, "Narrow-linewidth, tunable ultraviolet, Ti:sapphire laser for environmental sensing," *Applied Optics*, vol. 45, no. 10, pp. 2306-2309, April 2006.

[2]   A. Nehorai, B. Porat, and E. Paldi, "Detection and localization of vapor-emitting sources," *IEEE Transactions on Signal Processing*, vol. 43, no. 1, pp. 243-253, January 1995.

[3]   J. F. Federici, B. Schulkin, F. Huang, D. Gary, R. Barat, F. Oliveira, and D. Zimdars, "THz imaging and sensing for security applications-explosives, weapons and drugs," *Semiconductor Science and Technology*, vol. 20, no. 7, pp. S266-S280, July 2005.

[4]   U. Willer, M. Saraji, A. Khorsandi, P. Geiser, and W. Schade, "Near- and mid-infrared laser monitoring of industrial processes, environment and security applications," *Optics and Lasers in Engineering*, vol. 44, no. 7, pp. 699-710, July 2006.

[5]   Y. Pao, *Optoacoustic Spectroscopy and Detection*. New York: Academic Press, 1977.

[6]   I. Linnerud, P. Kaspersen, and T. Jaeger, "Gas monitoring in the process industry using diode laser spectroscopy," *Applied Physics B*, vol. 67, no. 3, pp. 297-305, September 1998.

[7]   M. M. J. W. van Herpen, S. Li, S. E. Bisson, and F. J. M. Harren, "Photoacoustic trace gas detection of ethane using a continuously tunable, continuous-wave optical parametric oscillator based on periodically poled lithium niobate," *Applied Physics Letters*, vol. 81, no. 7, pp. 1157-1159, August 2002.

[8]   T. Ritari, J. Tuominen, H. Ludvigsen, J. C. Petersen, T. Sorensen, T. P. Hansen, and H. R. Simônsen, "Gas sensing using air-guiding photonic bandgap fibers," *Optics Express*, vol. 12, no. 17, pp. 4080-4087, August 2004.

[9]   Y. L. Hoo, W. Jin, C. Shi, H. L. Ho, D. N. Wang, and S. C. Ruan, "Design and modeling of a photonic crystal fiber gas sensor," *Applied Optics*, vol. 42, no. 18, pp. 3509-3515, June 2003.

[10]   S. Schäfer, M. Mashni, J. Sneider, A. Miklós, P. Hess, H. Pitz, K. -U. Pleban, and V. Ebert, "Sensitive detection of methane with a 1.65 µm diode laser by photoacoustic and absorption spectroscopy," *Applied Physics B*, vol. 66, no. 4, pp. 511-516, April 1998.

[11]   P. Werle, F. Slemr, K. Maurer, R. Kormann, R. Mücke, and B. Jänker, "Near- and mid-infrared laser-optical sensors for gas analysis," *Optics and Lasers in Engineering*, vol. 37, n. 2-3, pp. 101-114, February-March 2002.

[12]   R. W. Fox, C. S. Weimer, L. Hollberg, and G. C. Turk, "The diode laser as a spectroscopic tool," *Spectrochimica Acta Reviews*, vol. 15, no. 5, pp. 291-299, 1993.

[13]   T. Hertsens, "An Overview of Laser Diode Characteristics," ILX Lightwave Application Note #5, July 2005;
http://www.ilxlightwave.com/appnotes/overview_laser_diode_characteristics.pdf

[14]   D. Romanini, M. Chenevier, S. Kassi, M. Schmidt, C. Valant, M. Ramonet, J. Lopez, and H. -J. Jost, "Optical-feedback cavity-enhanced absorption: a compact spectrometer for real-time measurement of atmospheric methane," *Applied Physics B*, vol. 83, no. 4, pp. 659-667, June 2006.

[15]   H. Li, G. B. Rieker, X. Liu, J. B. Jeffries, and R. K. Hanson, "Extension of wavelength-modulation spectroscopy to large modulation depth for diode laser absorption measurements in high-pressure gases," *Applied Optics*, vol. 45, no. 5, pp. 1052-1061, February 2006.

[16]   T. Le Barbu, B. Parvitte, V. Zéninari, I. Vinogradov, O. Korablev, and G. Durry, "Diode laser spectroscopy of H_2O and CO_2 in the 1.877-μm region for the in situ monitoring of the Martian atmosphere," *Applied Physics B*, vol. 82, no. 1, pp. 133-140, January 2006.

[17]   A. G. Hendricks, U. Vandsburger, W. R. Saunders, and W. T. Baumann, "The use of tunable diode laser absorption spectroscopy for the measurement of flame dynamics," *Measurement Science and Technology*, vol. 17, no. 1, pp. 139-144, January 2006.

[18]   C. S. Edwards, G. P. Barwood, H. S. Margolis, P. Gill, and W. R. C. Rowley, "High-precision frequency measurements of the $v_1 + v_3$ combination band of $^{12}C_2H_2$ in the 1.5 μm region," *Journal of Molecular Spectroscopy*, vol. 234, no. 1, pp. 143-148, November 2005.

[19]   W. Demtröder, *Laser Spectroscopy: Basic Concepts and Instrumentation*, 2nd ed., New York: Springer, 1996.

[20]   M. W. Sigrist, *Air Monitoring by Spectroscopic Techniques*. New York: Wiley, 1994.

[21]   Y. He, Z. Tang, Z. Chen, W. Wan, and J. Li, "A novel photoacoustic tomography based on a time-resolved technique and an acoustic lens imaging system," *Physics in Medicine and Biology*, vol. 51, no. 10, pp. 2671-80, May 2006.

[22]   M. Xu and L. V. Wang, "Photoacoustic imaging in biomedicine," *Review of Scientific Instruments*, vol. 77, no. 4, pp. 041101-1-041101-22, April 2006.

[23]   D. A. Hutchins and A. C. Tam, "Pulsed photoacoustic materials characterization," *IEEE Transactions on Ultrasonics, Ferroelectrics and Frequency Control*, vol. UFFC-33, no. 5, pp. 429-449, September 1986.

[24]   F. Zhang, S. Krishnaswamy, D. Fei, and D. A. Rebinsky, "Photoacoustic characterization of the mechanical properties of thin film materials," in *Testing, Reliability, and Application of Micro- and Nano-Material Systems III*, vol. 5766, no. 1, 89-98, May 2005.

[25]   V. P. Zharov and V. S. Letokhov, *Laser Optoacoustic Spectroscopy*. New York: Springer-Verlag, 1986.

[26]   M. Pushkarsky, A. Tsekoun, I. G. Dunayevskiy, R. Go, and C. K. N. Patel, "Sub-parts-per-billion level detection of NO_2 using room-temperature quantum cascade lasers," *Proceedings of the National Academy of Sciences of the United States of America*, vol. 103, no. 29, pp. 10846-10849, July 2006.

[27]   P. Russell, "Photonic crystal fibers," *Science*, vol. 299, no. 5605, pp. 358-362, January 2003.

[28]   BlazePhotonics datasheet; http://www.crystal-fibre.com/datasheets/HC19-1550-01.pdf

[29]   Y. L. Hoo, W. Jin, H. L. Ho, D. N. Wang, and R. S. Windeler, "Evanescent-wave gas sensing using microstructure fiber," *Optical Engineering*, vol. 41, no. 1, pp. 8-9, January 2002.

[30]   F. Benabid, F. Couny, J. C. Knight, T. A. Birks, and P. S. J. Russell, "Compact, stable and efficient all-fibre gas cells using hollow-core photonic crystal fibres," *Nature*, vol. 434, no. 7032, pp. 488-491, March 2005.

[31]   S. Firebaugh, "Miniaturization and integration of photoacoustic detection," Ph.D. Thesis, Department of Electrical Engineering and Computer Science, Massachusetts Institute of Technology, Cambridge, Massachusetts, June 2001.

[32]   J. Li, X. Gao, W. Li, Z. Cao, L. Deng, W. Zhao, M. Huang, and W. Zhang, "Near-infrared diode laser wavelength modulation-based photoacoustic spectrometer," *Spectrochimica Acta Part A*, vol. 64, no. 2, pp. 338-342, May 2006.

[33]   H. Wang, K. Williams, and W. Guan, "A vibrational mode analysis of free finite-length thick cylinders using the finite element method," *Journal of Vibration and Acoustics*, vol. 120, no. 2, pp. 371-377, April 1998.

[34]   BlazePhotonics datasheet; http://www.crystal-fibre.com/datasheets/HC-1550-02.pdf

[35]   S. D. Penn, A. Ageev, D. Busby, G. M. Harry, A. M. Gretarsson, K. Numata, and P. Willems, "Frequency and surface dependence of the mechanical loss in fused silica," *Physics Letters A*, vol. 352, nos. 1-2, pp. 3-6, March 2006.

91

[36] W. J. Startin, M. A. Beilby, and P. R. Saulson, "Mechanical quality factors of fused silica resonators," *Review of Scientific Instruments*, vol. 69, no. 10, pp. 3681-3689, October 1998.

[37] H. Zhang, W. Pang, H. Yu, and E. S. Kim, "High-tone bulk acoustic resonators on sapphire, crystal quartz, fused silica, and silicon substrates," *Journal of Applied Physics*, vol. 99, no. 12, pp. 124911-1-124911-5, June 2006.

[38] C. Zener, "Internal friction in solids. II. General theory of thermoelastic internal friction," *Physical Review*, vol. 53, no. 1, pp. 90-99, January 1938.

[39] A. M. Gretarsson and G. M. Harry, "Dissipation of mechanical energy in fused silica fibers," *Review of Scientific Instruments*, vol. 70, no. 10, pp. 4081-4087, October 1999.

[40] G. Harry, T. Corbitt, M. Freytsis, D. Ottaway, N. Mavalvala, and S. Penn, "Mechanical loss of laser-welded fused silica fibers," *Review of Scientific Instruments*, vol. 77, no. 2, pp. 023906-1-023906-3, February 2006.

[41] M. Weel and A. Kumarakrishnan, "Laser-frequency stabilization using a lock-in amplifier," *Canadian Journal of Physics*, vol. 80, no. 12, pp. 1449-1458, December 2002.

[42] W. C. Swann and S. L. Gilbert, "Pressure-induced shift and broadening of 1510-1540-nm acetylene wavelength calibration lines," *Journal of the Optical Society of America B*, vol. 17, no. 7, pp. 1263-1270, July 2000.

[43] http://wavelengthreferences.com

[44] J. Henningsen, J. Hald, and J. C. Petersen, "Saturated absorption in acetylene and hydrogen cyanide in hollow-core photonic bandgap fibers," *Optics Express*, vol. 13, no. 26, pp. 10475-10482, December 2005.

[45] N. Lagakos, E. U. Schnaus, J. H. Cole, J. Jarzynski, and J. A. Bucaro, "Optimizing fiber coatings for interferometric acoustic sensors," *IEEE Journal of Quantum Electronics*, vol. QE-18, no. 4, pp. 683-689, April 1982.

[46] A. T. Taylor, M. J. Matthewson, and C. R. Kurkjian, "Strength degradation of silica fibers by acetone immersion," presented at Optical Fiber Reliability and Testing, Boston, Massachusetts, September 1999.

[47] I. Ladabaum, X. Jin, H. T. Soh, A. Atalar, and B. T. Khuri-Yakub, "Surface micromachined capacitive ultrasonic transducers," *IEEE Transactions on Ultrasonics, Ferroelectrics and Frequency Control*, vol. 45, no. 3, pp. 678-690, May 1998.

[48] D. C. Abeysinghe, S. Dasgupta, J. T. Boyd, and H. E. Jackson, "A novel MEMS pressure sensor fabricated on an optical fiber," *IEEE Photonics Technology Letters*, vol. 13, no. 9, pp. 993-995, September 2001.

[49] A. Saran, D. C. Abeysinghe, and J. T. Boyd, "Microelectromechanical system pressure sensor integrated onto optical fiber by anodic bonding," *Applied Optics*, vol. 45, no. 8, pp. 1737-1742, March 2006.

[50] R. Thapa, K. Knabe, K. L. Corwin, and B. R. Washburn, "Arc fusion splicing of hollow-core photonic bandgap fibers for gas-filled fiber cells," *Optics Express*, vol. 14, no. 21, pp. 9576-9583, October 2006.

[51] R. Thapa, K. L. Corwin, and B. R. Washburn, "Splicing hollow-core photonic bandgap fibers to step-index fibers using an arc fusion splicer," presented at Conference on Lasers and Electro-Optics, Long Beach, California, May 2006.